

## MASTER

### Implementation of spin detection in a commercial low temperature scanning tunneling microscope

Keizer, J.G.

*Award date:*  
2007

[Link to publication](#)

#### **Disclaimer**

This document contains a student thesis (bachelor's or master's), as authored by a student at Eindhoven University of Technology. Student theses are made available in the TU/e repository upon obtaining the required degree. The grade received is not published on the document as presented in the repository. The required complexity or quality of research of student theses may vary by program, and the required minimum study period may vary in duration.

#### **General rights**

Copyright and moral rights for the publications made accessible in the public portal are retained by the authors and/or other copyright owners and it is a condition of accessing publications that users recognise and abide by the legal requirements associated with these rights.

- Users may download and print one copy of any publication from the public portal for the purpose of private study or research.
- You may not further distribute the material or use it for any profit-making activity or commercial gain

Eindhoven University of Technology  
Department of Applied Physics  
Photonics and Semiconductor Nanophysics Group

# Implementation of spin detection in a commercial low temperature scanning tunneling microscope

J.G. Keizer

December 2007

Under supervision of:  
dr. J.K. Garleff  
Prof. dr. P.M. Koenraad



# Abstract

In scanning tunneling microscopy (STM) the surface topography of an electrically conductive sample can be imaged with atomic resolution. In addition to imaging the surface topography, the local magnetization of the surface below the tip can be detected by making the tip sensitive to the spin of the tunneling current (SP-STM). In the current thesis progress toward the implementation of spin detection in a commercial STM is presented. The ultimate goal is to demonstrate that the information of the local magnetization can be extracted with an in house Omicron Low temperature STM through (1) direct measurement of the tunneling current and (2) by measuring the degree of circular polarization of the STM-induced luminescence. To show that the first method is feasible, the current thesis aims to replicate a well documented experiment in which thin layers of iron are deposited on a tungsten W(110) crystal. This approach requires a thorough cleaning of the W(110) surface, the ability to controllably deposit iron, and the creation of magnetic STM tips. In the current thesis, a detailed description is given on how the requirements of this method were fulfilled. The second method requires the development of an optical system to collect the STM-induced luminescence. To this end, a lens / fiber collection system that has been specially designed for the Omicron low temperature STM is tested.



---

# Contents

<b>0</b>	<b>Scope of the project</b>	<b>1</b>
<b>1</b>	<b>Introduction to spin polarized scanning probe microscopy</b>	<b>3</b>
<b>2</b>	<b>Theory of scanning tunneling microscopy</b>	<b>5</b>
2.1	Basic Concepts . . . . .	5
2.1.1	Tunneling . . . . .	5
2.1.2	Bardeen's formalism and the Tersoff-Hamann model . . . . .	9
2.1.3	Resolution limit . . . . .	12
2.2	Modes of operation . . . . .	13
2.2.1	Constant current mode . . . . .	14
2.2.2	Spectroscopy . . . . .	14
2.3	Spin-polarized tunneling . . . . .	16
2.3.1	Spin-polarized tunneling using magnetic probe tips . . . . .	16
2.4	STM-Induced luminescence . . . . .	20
2.4.1	Mechanisms of light emission . . . . .	20
2.4.2	Resolution limit . . . . .	22
2.4.3	Imaging of magnetic structures . . . . .	22
<b>3</b>	<b>Planned experiment</b>	<b>25</b>
<b>4</b>	<b>Scanning tunneling microscope</b>	<b>29</b>
<b>5</b>	<b>Thin film depositing</b>	<b>33</b>
5.1	Evaporator calibration . . . . .	33
5.2	Step flow growth . . . . .	37
<b>6</b>	<b>High temperature oven</b>	<b>39</b>
6.1	Materials . . . . .	39
6.2	Operational principle . . . . .	40
6.3	W(110) cleaning procedure . . . . .	41

<b>7</b>	<b>Tip preparation</b>	<b>45</b>
7.1	Etching . . . . .	45
7.2	In situ preparation . . . . .	47
7.3	Magnetic tips . . . . .	49
<b>8</b>	<b>Collection of STM-induced luminescence</b>	<b>53</b>
8.1	Lens selection . . . . .	53
8.2	Experimental validation . . . . .	55
<b>9</b>	<b>Conclusion &amp; outlook</b>	<b>61</b>
<b>10</b>	<b>Acknowledgments</b>	<b>63</b>
<b>A</b>	<b>Ray trace program</b>	<b>65</b>

## Chapter 0

# Scope of the project

In the current report the progress that has been made toward the upgrade of a low temperature conventional scanning tunneling microscope (STM) to a spin-polarized scanning tunneling microscope (SP-STM) is presented. Although conventional STM setups are routinely used by numerous groups, institutions, and businesses around the world, only ten SP-STM are in operation globally at the moment. The reason for this seemingly low number are the numerous experimental difficulties that one encounters when attempting to upgrade an STM to an SP-STM; some of the groups took ten years or more to get to the point that they were able to routinely perform SP-STM. In sharp contrast, the time frame of the current project was less than a year. In the view of the fact that others sometimes needed 10 years or more to demonstrate SP-STM, the set time frame was quite a challenge for this group that has no SP-STM experience. To avoid most pitfalls, the current project follows the well documented approach of the Hamburg group to demonstrate SP-STM. However, the fact that a well documented approach is followed does by no means imply that no experimental difficulties remain. As it turns out, this project consisted primarily of solving the numerous experimental problems. One might be tempted to think that the goal might be too ambitious in the given time frame. However, as will be explained in detail in this report, there is good reason to believe that all the major experimental difficulties have been overcome and that everything is in place to demonstrate spin-polarized scanning tunneling microscopy. In fact, if it was not for a malfunction of the STM itself in the final weeks of this project, spin-polarized scanning tunneling microscopy would probably have been successfully demonstrated. Although the successful demonstration of SP-STM would have been the crowning glory on all the work done during this master thesis, much was learned in the course of this project and it will be a matter of limited time before SP-STM will be achieved.





## Chapter 1

# Introduction to spin polarized scanning probe microscopy

Since its invention by Binnig and Rohrer [1–4] in the early 1980s, the scanning tunneling microscope (STM) has become a versatile tool in various fields such as condensed matter and material science. In STM an atomically sharp tip is positioned by piezoelectric actuators above the surface of interest. When the distance between the electrically conducting sample and the tip is sufficiently small, the application of a small voltage between sample and tip will lead to a quantum mechanical tunneling current. This tunneling current decays exponentially with increasing distance between sample and tip by an order of magnitude per angstrom. Since typical lattice constants are in the order of several angstroms, the tunneling current will primarily flow through the outermost atom of an atomically sharp tip. By keeping the tunneling current constant by means of a feedback loop while scanning the tip laterally above the sample surface, a topographic image of the sample surface can be obtained with atomic resolution.

The field of nanotechnology proved to be an important field that was highly stimulated by the introduction of STM. As it turned out, an STM allows one to manipulate matter down to the atomic scale [5–7]. In 1959, Richard Feynman already foresaw the enormous potential of manipulating structures at the atomic scale in his famous talk “*There’s Plenty of Room at the Bottom*” [8]. With the invention of the STM by Binnig and Rohrer twenty three years later a tool with which his vision could be realized was introduced. Since then, STM has opened the way to the construction and manipulation of atomic scale devices [9, 10]. Furthermore, the invention of the STM has triggered the development of various related scanning probe microscopy techniques (SPM) which can be used to probe almost any kind of interaction with a least sub-micrometer resolution. It is therefore not surprising that nowadays the SPM is being routinely used in other fields, e.g. electrochemistry and biology, as well.

In 1988, Pierce [11] proposed to investigate the local magnetization of the

surface below the apex of an STM tip by making the tip sensitive to the spin of the tunneling current. In principle, this would mean that the magnetic domain structure of a sample can be imaged with ultimate resolution down to the atomic scale. The atomic scale spatial resolution that this technique provides is highly desirable for answering some fundamental questions in surface science. Although there has been an established technique for probing magnetic surface in the form of magnetic force microscopy since the 1990s [12, 13], this technique lacks the sensitivity and atomic scale spatial resolution of spin-polarized scanning tunneling microscopy (SP-STM). Currently, SP-STM is the most powerful tool to study the interplay between structural, electronic, and magnetic properties on the nanoscale [14, 15].

Obtaining surfaces with known or predictable magnetic variations on the atomic scale has been part of the difficulty of establishing SP-STM on the atomic scale as a reliable technique. A slightly miscut tungsten crystal covered with a thin film of iron is one of the samples of which the variation in the direction of magnetization is known. It was found by the Hamburg group [16] that in thin layers of iron on the tungsten W(110) surface the direction of magnetization will alternate from in-plane to out-of-plane on the nanometer scale, resulting in high magnetic contrast in the acquired image. For this reason, and the fact that the approach is well documented, the current project aims to replicate the Hamburg approach to demonstrate SP-SPM in the in house Omicron low temperature STM.

The outline of the thesis is as follows; in the first part, chapter 2, the basics and the theory of (SP)-STM is thoroughly examined. The second part of this reports, chapter 3–8, deals with all the experimental details, the encountered problems, the solutions, and the intermediate results. The report is concluded, chapter 9, with a summary of all the obtained results and a brief outlook to the future.

## Chapter 2

# Theory of scanning tunneling microscopy

### 2.1 Basic Concepts

#### 2.1.1 Tunneling

As mentioned in the introduction, scanning tunneling microscopy is made possible by the quantum mechanical effect of tunneling. In this section a simple one-dimensional model that describes the process of electron tunneling through a potential barrier is presented.

In the classical regime, i.e. the regime in which the involved length scales can be considered as macroscopic, the motion of particles is governed by Newton's second law,  $f = ma$ , and conservation of energy. For most applications this proves to be an accurate physical description. However, at atomic and subatomic length scales Newton's second law ceases to explain the observed phenomenon and the theory of quantum mechanics is required to describe the behavior of particles. At the heart of the theory of quantum mechanics stands Schrödinger's equation which plays the role of Newton's second law and conservation of energy in classical mechanics.

Before modeling the more complex situation of electrons tunneling between a sample and the tip of an STM, the simplified situation of the piece-wise-constant potential depicted in figure 2.1 is investigated. In the framework of quantum mechanics the state of an electron with energy  $E$  moving in a potential  $\phi$  is described by a wave function  $\psi(z)$  which has to satisfy the time-independent Schrödinger equation:

$$-\frac{\hbar^2}{2m} \frac{d^2}{dz^2} \psi(z) + \phi(z)\psi(z) = E\psi(z) \quad (2.1)$$

in which  $m$  the electron mass,  $\hbar = 1.054 \times 10^{-34}$  Js the reduced Planck constant, and  $z$  the position coordinate. In the classically allowed regions of the piece-

wise-constant potential the solutions of Schrödinger's equation are given by:

$$\psi(z) = \psi(0)e^{\pm ikz} \quad (2.2)$$

with  $k$  the wave vector given by:

$$k = \frac{\sqrt{2m(E - \phi)}}{\hbar}. \quad (2.3)$$

These solutions represent an electron moving in either positive or negative direction with constant momentum, just as one would expect in the classical regime. In the classically forbidden region of the piece-wise-constant potential the solutions of Schrödinger's equation are given by:

$$\psi(z) = \psi(0)e^{\pm \kappa z} \quad (2.4)$$

with  $\kappa$  the decay constant given by:

$$\kappa = \frac{\sqrt{2m(\phi - E)}}{\hbar}. \quad (2.5)$$

This solution describes a state of an electron penetrating the potential barrier with a decaying wave function. The probability  $w$  of observing an electron near a point  $z$  is in Born's statistical interpretation of quantum mechanics given by:

$$w \propto |\psi(z)|^2 = |\psi(0)|^2 e^{\pm 2\kappa z} \quad (2.6)$$

which has, in contrast to the solution of the equation of motion in classical mechanics, a nonzero value in the barrier region; the electron has a nonzero probability to penetrate, or so to speak tunnel through, the potential barrier.

The elementary piece-wise-constant potential model described above can be extended to explain the basic features of the metal-vacuum-metal junction found in an STM. In order to model the tunneling of electrons between sample and the tip of an STM, two simplifications are made. Firstly, the tunneling of electrons is assumed to be elastic, i.e. the energy of the electrons is conserved, implying that the initial and final states have the same energy. One should note however, that there exist indeed inelastic tunneling processes in which the energy of the initial and final state may differ, e.g. processes in which a phonon or photon is involved. Secondly, the work function  $\phi$ , defined as the minimum energy required to remove an electron from the bulk to the vacuum level, is assumed equal for both metallic sample and tip.

In figure 2.2a, an one-dimensional tunnel junction consisting of a sample and a tip over which no bias voltage is applied is schematically depicted. In this representation, both sample and tip are modeled as semi-infinite pieces of free-electron metal with the same Fermi level. The Fermi level  $E_F$  is, with neglect of the thermal excitation, the upper limit of the occupied states in a metal and can, if the vacuum level is taken as the energy reference point, be expressed

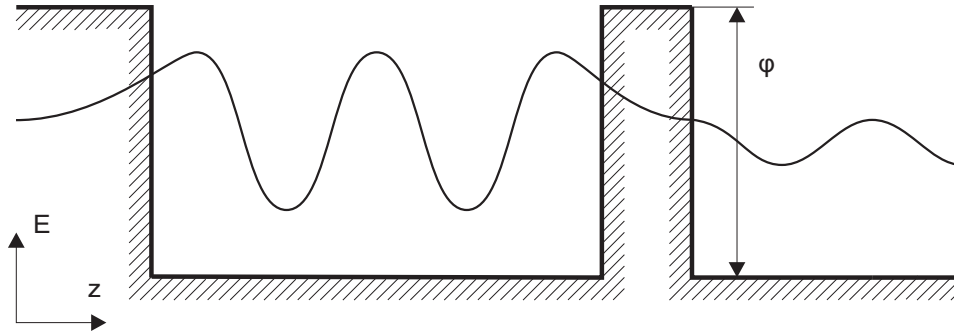


**Figure 2.1:** Qualitative structure of the wave function of an electron tunneling through a piece-wise-constant potential barrier. As can be seen, the wave function extends into the classically forbidden region and exits with a nonzero amplitude on the other side of the potential barrier.

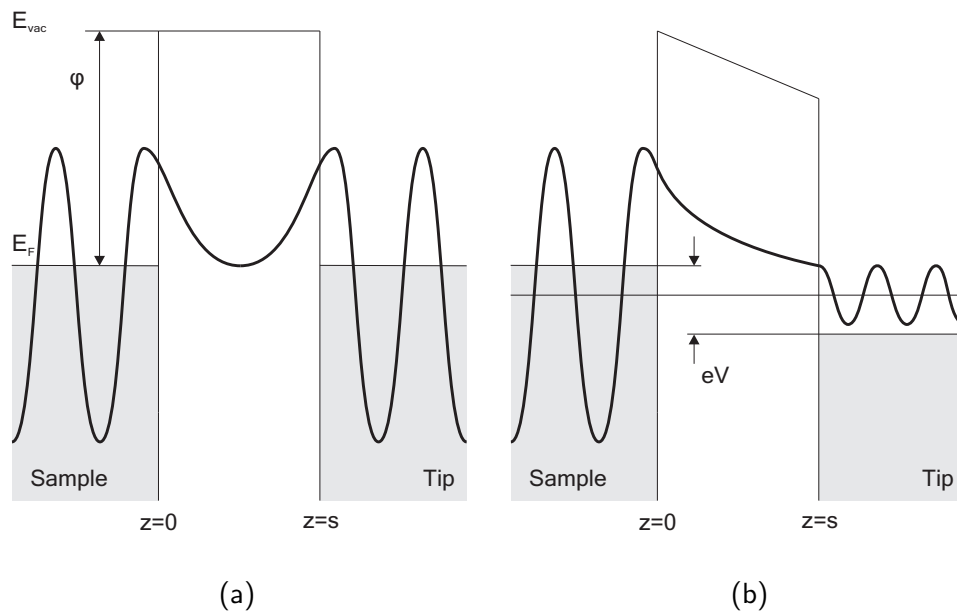


**Figure 2.2:** Schematic representation of an one-dimensional metal-vacuum-metal tunneling junction as found in an STM, with (a) no bias voltage and (b) an negative bias voltage applied. The sample (left) and the tip (right) are modeled as two semi-infinite pieces of free-electron metal. In both cases the wave functions of the electrons in tip and sample overlap, but only when a bias voltage is applied the electrons will have a preferential tunneling direction resulting in a net tunneling current. In the case depicted in (b) the electrons will tunneling from filled states of the sample into empty states of the tip.

as  $E_F = -\phi$ . Analogous to the case of the piece-wise-constant potential, the electrons in the sample can tunnel through the potential barrier into the tip and *vice versa*. However, since no bias voltage is applied, there exists symmetry with respect to the vacuum gap and electrons will have no preference in tunneling from the sample to the tip or *vice versa*, resulting in no net tunneling current.

In case a bias voltage  $V$  is applied, see figure 2.2b, the Fermi level on one side of the vacuum gap can, depending on the polarity of the bias, be raised or lowered. Subsequently, the symmetry will be broken and more electrons will tunnel through the barrier in one direction, resulting in a net tunneling current. Depending on the polarity of the bias voltage, a state  $\psi_n$  with an energy level  $E_n$  lying between  $E_F - eV$  and  $E_F$  can tunnel from the tip into an empty state of the sample or from the sample into an empty state of the tip. If the bias voltage is assumed much smaller than the value of the work function,  $eV \ll \phi$ , all the sample states of interest will be close to the Fermi level, that is,  $E_n \approx -\phi$ . The probability  $w$  for an electron in the  $n$ th sample state to be present at the surface of the tip is then, analogue to equation (2.6), given by:

$$w \propto |\psi_n(0)|^2 e^{-2\kappa s} \quad (2.7)$$

in which  $\psi_n(0)$  is the value of the  $n$ th sample state at the sample surface,  $s$  the size of the vacuum gap between sample and tip, and

$$\kappa = \frac{\sqrt{2m\phi}}{\hbar} \quad (2.8)$$

the decay constant in the barrier region of a sample state near the Fermi level. Equation (2.7) is an expression for the probability of an electron being present at the surface of the tip for a single state. The total tunneling current can be obtained by including all the sample states in the energy interval  $eV$  and is given by:

$$I \propto \sum_{E_n=E_F-eV}^{E_F} |\psi_n(0)|^2 e^{-2\kappa s}. \quad (2.9)$$

In case the density of the electronic states does not change significantly with the applied bias voltage, equation (2.9) can be expressed in terms of the local density of states (LDOS) at the Fermi level. A sample's LDOS at a location  $z$  and energy  $E$  is defined as:

$$\rho_S(z, E) \equiv \frac{1}{\epsilon} \sum_{E_n=E-\epsilon}^E |\psi_n(z)|^2 \quad (2.10)$$

for a sufficiently small energy interval  $\epsilon$ . The tunneling current, equation (2.9), can be then be rewritten in terms of the LDOS of the sample as:

$$I \propto V \rho_S(0, E_F) e^{-2\kappa s} \approx V \rho_S(0, E_F) e^{-1.025 \sqrt{\hat{\phi}} \hat{s}} \quad (2.11)$$

with  $\hat{\phi}$  the numerical value of the barrier height in eV, and  $\hat{s}$  the numerical value of the distance between sample and tip in angstrom units.

### 2.1.2 Bardeen's formalism and the Tersoff-Hamann model

The model of the tunneling current described in section (2.1.1) is valid for one dimension. However, STM is sensitive to the full three-dimensional structure of the surface of both sample and tip. A theory of STM which takes into account the three-dimensional structure of tip and sample has been developed by Tersoff and Hamann [17]. In their model, Tersoff and Hamann approximate the wave functions of the tip by a spherical  $s$ -wave function, see figure 2.3. By making use of the so-called transfer Hamiltonian approach, first introduced by Bardeen [18] to explain current vs. voltage curves of oxide barriers between two superconductors, Tersoff and Hamann were able to derive an expression for the tunnel current in STM. The result is a theory which has the advantage that it is sufficiently realistic to permit quantitative comparison with experimental images, and yet is sufficiently simple that its implementation is straightforward.

In the Bardeen approach to tunneling two separate free subsystems, as schematically depicted in figure 2.4, are considered first. The electronic states of these two free subsystems can be obtained by solving the stationary Schrödinger equations. Subsequently, the rate of electron transfer from one electrode to the other can be calculated by time-dependent perturbation theory [19]. Using this theory, Bardeen showed that the amplitude of electron transfer, or tunneling matrix element  $M$ , is determined by the overlap of the surface wave functions of the two free subsystems and is given by:

$$M = \frac{\hbar}{2m} \int_{z=z_0} \left( \psi_\mu^* \frac{d\psi_\nu}{dz} - \psi_\nu \frac{d\psi_\mu^*}{dz} \right) ds \quad (2.12)$$

in which  $\psi_{\mu,\nu}$  the wave functions of the two electrodes, and  $z_0$  the  $z$ -position of an arbitrary surface between the two electrodes.

Given the matrix element  $M$ , the rate of electron transfer can then be determined by using Fermi's golden rule [20], which states that an electron in state  $\psi_\mu$  at energy level  $E_\mu$  has a probability  $w$  of tunneling to a state  $\psi_\nu$  of energy  $E_\nu$  given by:

$$w = \frac{2\pi}{\hbar} |M|^2 \delta(E_\mu - E_\nu). \quad (2.13)$$

The  $\delta$ -function in equation (2.13) indicates that the only tunneling process considered is that of elastic tunneling, i.e. tunneling of electrons between the two electrodes is only supported by states with the same energy level.

An expression for the tunneling current can be obtained by summing equation (2.13) over all relevant states and the result is given by:

$$I = \frac{2\pi e}{\hbar} \sum_{\mu,\nu} f(E_\mu) [1 - f(E_\mu + eV)] |M|^2 \delta(E_\mu - E_\nu) \quad (2.14)$$

or expressed in the more commonly used integral form:

$$I = \frac{4\pi e}{\hbar} \int_{-\infty}^{\infty} [f(E_F - eV + \epsilon) - f(E_F + \epsilon)] \rho_\mu(E_F - eV + \epsilon) \rho_\nu(E_F + \epsilon) |M|^2 d\epsilon \quad (2.15)$$



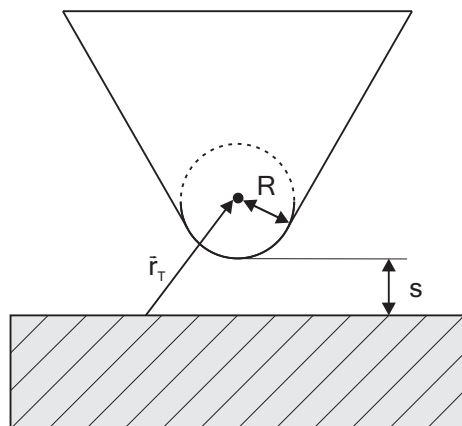


**Figure 2.3:** Schematics of the Tersoff-Hamann model. The probe tip has arbitrary shape but is assumed locally spherical with radius of curvature  $R$  at the point where it approaches nearest the surface. The position of the tip's center of curvature is given by  $\vec{r}_T$  at a minimum distance  $z = R + s$  from the sample surface. Only the  $s$ -wave solution of the spherical-potential-well problem is taken as the tip wave function.

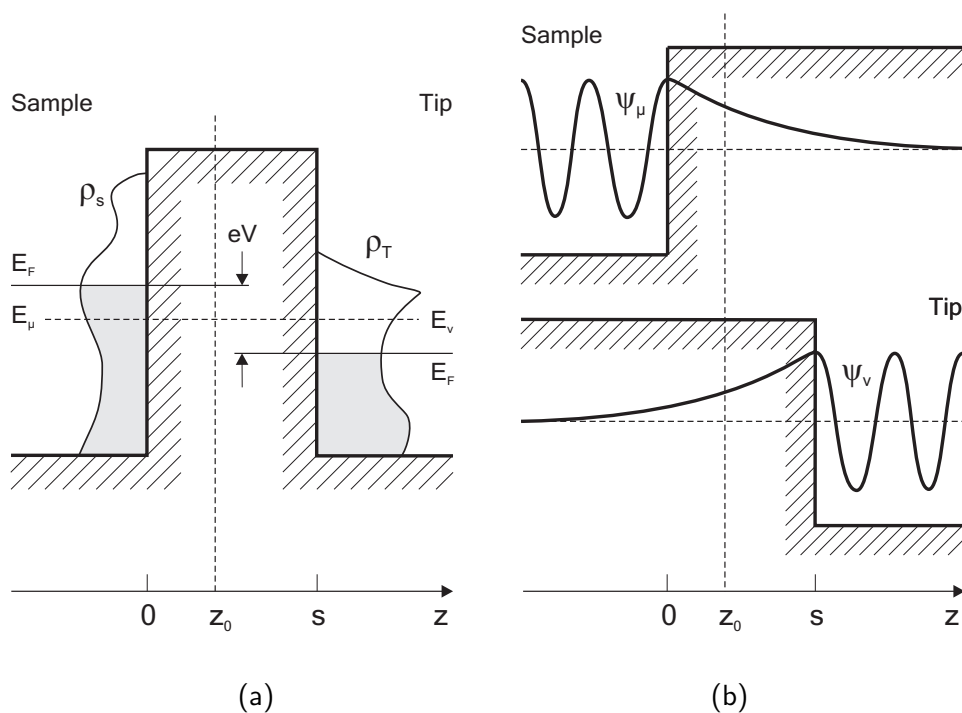


**Figure 2.4:** The Bardeen approach to tunneling theory. Instead of solving the Schrödinger equation for the coupled system (a), Bardeen [18] makes use of perturbation theory. Taking the two free subsystems (b) as a starting point, the tunneling current is calculated through the overlap of the wave functions of the two free systems using the Fermi's golden rule.

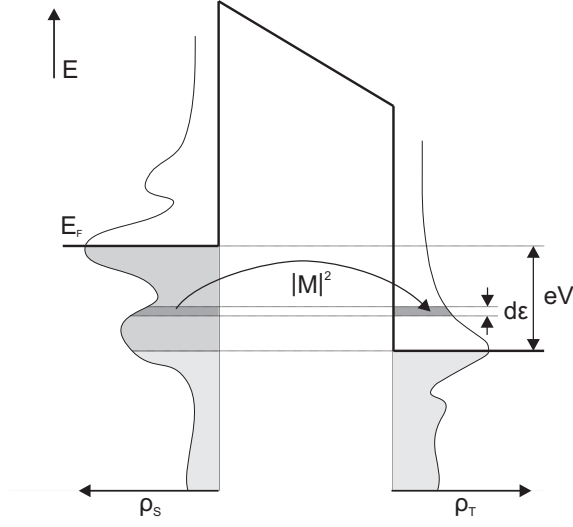


**Figure 2.5:** Schematic representation of elastic tunneling in an STM. Tunneling is only possible in the energy interval from  $E_F$  to  $(E_F - eV)$ . Within this energy interval tunneling is only possible to states with a corresponding energy (arrow). The strength of the tunneling from one state to a corresponding state is a function of the density of states of sample, tip, and the matrix element  $M$ . The total tunneling current can be obtained by integrating over the energy interval  $E_F$  to  $(E_F - eV)$ .

in which  $f$  the Fermi function given by:

$$f(E) = \frac{1}{1 + e^{\frac{E - E_F}{k_b T}}} \quad (2.16)$$

with  $T$  the temperature, and  $k_b$  Boltzmann's constant. In the limit of low temperatures and low applied bias voltage, equation (2.14) reduces to:

$$I = \frac{2\pi}{\hbar} e^2 V \sum_{\mu, \nu} |M|^2 \delta(E_\mu - E_F) \delta(E_\nu - E_F). \quad (2.17)$$

or expressed in integral form:

$$I = \frac{4\pi e}{\hbar} \int_0^{eV} \rho_\mu(E_F - eV + \epsilon) \rho_\nu(E_F + \epsilon) |M|^2 d\epsilon \quad (2.18)$$

In combination with figure 2.5, which shows a schematic representation of the process of tunneling in an STM, the integral equations (2.15) and (2.18) have the advantage that they provide a clear and simple understanding of the tunneling process.

Starting from equation (2.17), Tersoff and Haman continued to show that in case a  $s$ -wave approximation is used for the wave functions  $\psi_\mu$  of the tip the expression for the tunneling current takes the following form [17]:

$$I \propto V \rho_T(E_F) e^{2\kappa R} \sum_{\nu} |\psi_\nu(\vec{r}_T)|^2 \delta(E_\nu - E_F) \quad (2.19)$$

with  $\kappa$  the decay constant given by equation (2.5),  $\vec{r}_T$  the center of curvature of the tip,  $\rho_T(E_F)$  the LDOS of the tip at the Fermi level, and  $R$  the effective tip radius as defined in figure 2.3. The right hand side quantity given by:

$$\sum_{\nu} |\psi_\nu(\vec{r}_T)|^2 \delta(E_\nu - E_F) = \rho_S(\vec{r}_T, E_F) \quad (2.20)$$

can, conform equation (2.10), be identified as the LDOS at the Fermi level of the sample, i.e. the charge density from the electronic states at  $E_F$  evaluated at the center of curvature  $\vec{r}_T$  of the tip. Since the sample wave functions  $\psi_\nu$  decay exponentially in the  $z$ -direction normal to the surface:

$$\psi_\nu(\vec{r}_T) \propto e^{-\kappa z} \quad (2.21)$$

we find that:

$$|\psi_\nu(\vec{r}_T)|^2 \propto e^{-2\kappa(s+R)}. \quad (2.22)$$

Substituting this result into equation (2.19) yields in case of a flat LDOS tip a tunneling current of:

$$I \propto V \rho_S(0, E_F) e^{-2\kappa s}. \quad (2.23)$$

Apparently, the tunneling current given by the three-dimensional Tersoff-Hamann model shows the same exponential dependence on the distance  $s$  between sample and tip as in the one-dimensional tunneling theory presented in section (2.1.1).

The Tersoff-Hamann model presented above constitutes of an elegant first-order model of STM that allows for a good introduction into the basics of STM. Although extensions of the Tersoff-Hamann model can be found in literature, e.g. wave-vector-dependent tunneling calculations by Baratoff [21] and inclusion of  $d$ -wave functions by Chen [22], the Tersoff-Hamann model is due to its simplicity still regarded as the standard model for STM.

### 2.1.3 Resolution limit

At the beginning of their experiments, Binnig and Rohrer made an estimate of the lateral resolution that could be achieved in STM. Their original argument was reproduced by [23] and is schematically shown in figure 2.6a. In case the distance between the apex of the tip and the sample surface is much smaller than the tip radius, the current lines will be almost perpendicular to the surface. Under the assumption that the tunneling current density at each point will be governed by the formula for the one-dimensional tunneling case, equation (2.11), the lateral current distribution will be given by:

$$I(\Delta x) = I_0 \exp\left(-2\kappa \frac{\Delta x^2}{2R}\right). \quad (2.24)$$

Evaluation of this equation shows that the tunneling current is concentrated in a small circle with a radius of 45 Å for a tip with a radius of 1000 Å. For a tip radius of 100 Å, the area in which the tunneling current is concentrate is reduced to only 14 Å. This arguments shows that potentially a very high resolution can be obtained in STM. In reality, the lateral resolution that can be achieved in STM is found to greatly exceed this expectation; details of surface structures with a spatial resolution of 2 Å are routinely observed, giving STM an atomic resolution.

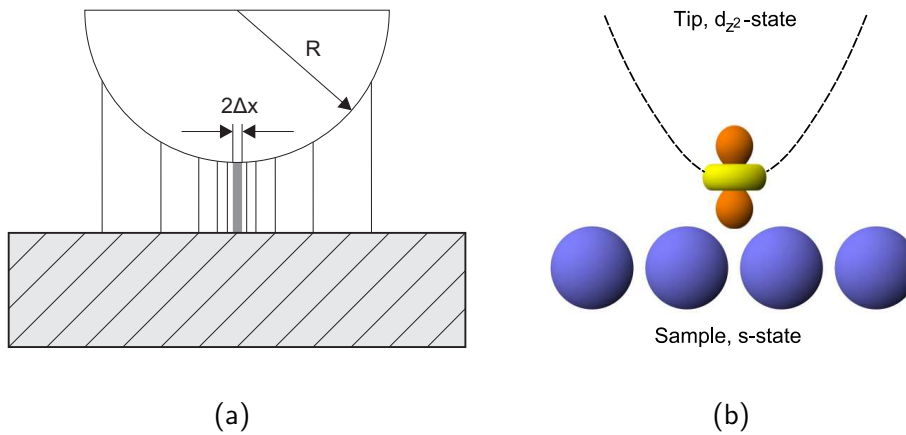


**Figure 2.6:** (a) Binnig's and Rohrer's original estimation of the lateral resolution in STM. In case the distance between the apex of the tip and the sample surface is much smaller than the tip radius  $R$ , the current lines will be almost perpendicular to the surface. The tunnel current density will drop off very rapidly as a function of lateral position and will therefore be concentrated in a small region,  $2\Delta x$ , around the origin:  $R = 100 \text{ \AA}$  results in  $\Delta x = 14 \text{ \AA}$ . (b) Schematic representation of a tip with the outermost atom in a  $d_{z^2}$ -state. The sharp protrusion of the  $d_{z^2}$ -state results in atomic resolution.

The original  $s$ -wave model of Tersoff and Hamann fails, at least on metals, in explaining the atomic resolution of STM. The reason for this is that in the model the tip is portrayed as a potential well with a local curvature. The  $s$ -wave model does not include the actual electronic states of the tip and is thus not a valid model for the most commonly used tip materials: W, Pt, and Ir, which are  $d$ -band metals. For tungsten tips 85% of the density of states at the Fermi level comes from the  $d$  states [24]. In this case, the majority of states at the Fermi level will not have the  $s$ -type symmetry as suggested by Tersoff and Hamann. Rather, these states with higher angular momentum will have a more complex shape. For example, the tip state of a tungsten tip has the tendency to be dominated by a highly localized metallic  $d_{z^2}$ -dangling bond. In figure 2.6b, the shape of such a  $d_{z^2}$ -state on the end of a tungsten tip above a  $s$ -state sample surface, e.g. Au, is schematically depicted. As can be seen, the  $d_{z^2}$ -state has a sharp protrusion in the direction perpendicular to the sample surface. It is this sharp shape of the  $d_{z^2}$ -state that makes the atomic resolution that is routinely observed in STM possible.

## 2.2 Modes of operation

Imaging of a surface by means of STM can be done in two main modes of operation: constant current mode, see section (2.2.1) or constant height mode. Since in the current report only the current mode is used, and the constant

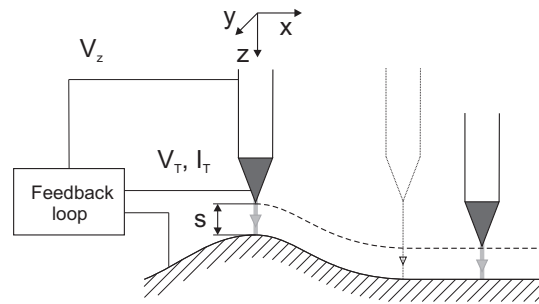


**Figure 2.7:** Schematic representation of the constant current mode of operation in STM. In this mode the distance between the sample and tip is kept constant by means of a feedback loop.

height mode has in general little application, only the former will be discussed. In addition to these two topographic modes, it is possible to directly probe the electronic structures of materials at an atomic level by e.g. spatially resolved tunneling spectroscopy. Spectroscopy will be introduced in section (2.2.2).

### 2.2.1 Constant current mode

In figure 2.7a, the principle of the constant current mode of operation is schematically depicted. As the name of this mode of operation implies, the tunneling current is kept constant by means of a feedback loop coupled to the  $z$ -piezo while scanning the tip over the surface. In this way, the acquired image can be thought of as a topographic map of the surface. i.e.  $z(x, y)$ . However, one has to be carefully using the term “topography” in relation to the constant current mode. The obtained image in constant current mode is related to the energy integrated LDOS of the sample or in the case of small bias voltages to contours of constant LDOS at the Fermi level, as explained in section (2.1.2). The main advantage of the constant current mode of operation is that it provides the most robust way to image surfaces which are not atomically flat. A disadvantage of the constant current mode of operation is the finite response time of the feedback loop which imposes relative low limits on the maximum attainable scan speed.

### 2.2.2 Spectroscopy

In the constant current mode of operation, an STM measurement will yield the energy integrated LDOS of the sample which to first approximation corresponds to the topography of the surface. In addition to the topographic information extracted by this method of operation, tunneling spectroscopy gives access to the chemical and electronic properties of the surface under investigation. Experimentally, tunneling spectroscopy means that one of the externally adjustable parameters ( $I, V$ ) is varied while keeping the others constant. The main merits of tunneling spectroscopy performed with an STM are [25]:

- It is local.
- It is performed at preselected positions.

- It is performed under well-defined conditions.
- It can be combined with other methods.
- it can provide spectroscopic images.

One experimental method of extracting spectroscopic information is  $I$ - $V$  spectroscopy. In this method,  $I$ - $V$  curves are obtained by measuring the variation of the tunneling current as a function of the voltage at a constant tip-sample separation. This technique requires the addition of a sample-and-hold circuit to the feedback loop. The sample-and-hold circuit interrupts the feedback loop while holding the tip position stable for a given time of the measurement. Subsequently, the bias voltage is ramped while the tunneling current is simultaneously measured. The tunneling bias voltage is then reset to its original value and the feedback loop is reengaged. By numerically taking the derivative of the acquired  $I$ - $V$  curves, the spectroscopic information as a function of the applied voltage can be obtained.

The experimental spectroscopic method described above can be combined with the scanning capability of an STM, resulting in high-spatial-resolution spectroscopy measurements. One way to generate a spectroscopic image is scanning the STM across the surface in constant current mode while taking a spectrum at each image point (current imaging tunneling spectroscopy, CITS). The major advantages of CITS is that all the spectroscopic information for one image point is taken at the same time, thereby reducing problems associated with sample drift and tip instabilities encountered in case the spectroscopic information were to be extracted from a set of topographic images that were taken in sequence. However, this way of obtaining spectroscopic information can still take a long time and as a result the associated problems of sample drift and tip instabilities are by no means completely eliminated.

An alternative and more targeted way of obtaining spectroscopic information is by adding a small AC-component to the DC bias voltage. The frequency of the AC-component is chosen such that it is too fast for the feedback loop to respond to it. By measurement of the current modulation at the frequency of the impose AC-component with use of a lock-in amplifier,  $dI/dV$  at the fixed bias voltage  $V$  can be measured. The disadvantage of this instrumental method is that it yields spectroscopic information at the single fixed bias voltage only. However, if the voltage of interest is known beforehand, e.g. by previous measurements, this method requires far less time to obtain a  $dI/dV$  image than in case a complete spectrum is taken at every image point. In this was the problems associated with sample drift and tip instabilities can be reduced to a minimum.

On of the most interesting properties that can be determined by means of  $I$ - $V$  spectroscopy is the LDOS of the sample as a function of the energy. Under the assumption of a tip with a constant DOS, taking the derivative of the tunneling current, equation (2.18), with respect to  $V$  results in a conductance

that is proportional to the LDOS of the sample:

$$\frac{dI}{dV}(V) \propto \rho_S(\vec{r}_T, E_F + eV). \quad (2.25)$$

Thus, by taking the derivative of the  $I$ - $V$  curves or by measuring the  $dI/dV$  signal directly, the LDOS of the sample can be probed relatively easily.

## 2.3 Spin-polarized tunneling

In 1925 G.E. Uhlenbeck and S. Goudsmit, working as P. Ehrenfest's assistants at the University of Leiden, proposed the concept of elementary particle spin [26]. Experimental evidence of the fine structure of hydrogen and the Stern-Gerlach experiment suggested an additional intrinsic electron property next to the then known electron's properties of mass and charge. Both these experiments could be explained by the possession of intrinsic angular momentum and magnetic moment by individual electrons. In a classical view this corresponds to the electron being a spinning ball of charge, from which the proposed property derived its name: spin. Nowadays, electron spin is considered to be a quantum mechanical property with the dimension of angular momentum, which can take two values  $+\frac{1}{2}$  (up,  $\uparrow$ ) and  $-\frac{1}{2}$  (down,  $\downarrow$ ) along the quantization axis.

Soon after the introduction of the STM it was realized that the intrinsic particle property of spin can be exploited in scanning tunneling microscopy (SP-STM) to measure the local magnetization of the surface below an STM-tip [27]. Historically, three different methods are used to obtain the spin-polarized electrons at or close to the Fermi level that are required for spin-polarized tunneling:

- The Zeeman splitting of a BCS-like superconductor in an external magnetic field [28].
- Optical pumping of GaAs with circularly polarized light [29].
- The intrinsic exchange-splitting of (anti)ferro-magnetic material [16].

In the current report only the last option which includes the use of a ferromagnetic tip in the STM, first proposed by Pierce [11], is pursued to generate the required spin-polarized electrons.

### 2.3.1 Spin-polarized tunneling using magnetic probe tips

As mentioned above, using two spin-polarized electrodes, e.g. two ferromagnetic materials, is one way to obtain the for spin-polarized tunneling microscopy required spin-polarized electrons at the Fermi level. In ferromagnetic materials the electron bands can spontaneously split into spin-up and spin-down bands if the relative gain in exchange interaction is larger than the loss in kinetic energy as described by the Stoner model [30]. The relative shifting of the two spin

bands will result in a different composition and magnitude of the total spin-dependent density of states at the Fermi-level. Whether a spin band is shifted up or down in energy depends on its magnetic quantization axis, i.e. the spin band with the spin aligned with the magnetic quantization axis will shift to a lower energy whereas the spin band with its spin anti-aligned will shift to a higher energy. In case of elastic tunneling where the spin is a conserved property, the total tunneling current between two electrodes will thus be influenced by the relative orientation of their magnetic quantization axis. For a system consisting of two identical ferromagnetic electrodes, the splitting into spin-up and spin-down bands and the subsequent influence on the tunneling current is for the two extreme situations of parallel and anti-parallel magnetization illustrated in figure 2.8. The relative shifting of the spin-up and spin-down bands results in a spin polarization at the Fermi level given by:

$$P_{T,S}(E_F) = \frac{\rho_{T,S}^{\uparrow}(E_F) - \rho_{T,S}^{\downarrow}(E_F)}{\rho_{T,S}^{\uparrow}(E_F) + \rho_{T,S}^{\downarrow}(E_F)}. \quad (2.26)$$

As can be seen in figure 2.8, the total tunneling current depends on the degree of polarization of both sample and tip, and the relative orientation of their magnetic quantization axis. To quantify the change in tunneling current and derive an expression for the spin-polarized tunneling current, Heinze and Wortmann [31, 32] extended the *s*-wave model of Tersoff and Hamann to include spin-polarized tunneling. Analog to the Tersoff and Hamann model, Heinze and Wortmann assumed the spin-up and spin-down DOS of the tip to be constant in energy but different in size to account for the magnetization of the tip. Under further assumption of low temperature and small bias voltage, the spin-polarized tunneling current they derived is given by:

$$I(\vec{r}_T, V, \theta) \propto \rho_T \tilde{\rho}_S(\vec{r}_T, E_F + eV) + \vec{m}_T \vec{m}_S(\vec{r}_T, E_F + eV) \quad (2.27)$$

with  $\tilde{\rho}_S$  and  $\vec{m}_S$  respectively the integrated local DOS and the vector of the energy integrated local magnetization DOS of the sample. The latter is given by an energy integral of the local magnetization DOS:

$$\vec{m}_S(\vec{r}_T, E_F + eV) = \int \vec{m}_S(\vec{r}_T, \epsilon) d\epsilon. \quad (2.28)$$

The spin-polarized tunneling current given by equation (2.27) can, by means of the definition of the polarization given by equation (2.26), be rewritten as [33, 34]:

$$I(\vec{r}, V, \theta) = I_0 + I_{sp} = I_0[1 + P_T P_S \cos(\vec{M}_T, \vec{M}_S)] \quad (2.29)$$

in which  $I_0$  the conventional tunneling current of non-spin-polarized electrons,  $I_{sp}$  the tunnel current of spin-polarized electrons, and  $\theta = \cos(\zeta) \cos(\varphi) = (\vec{M}_T, \vec{M}_S)$  the angle between the magnetic quantization axis of sample and tip as defined in figure 2.9.



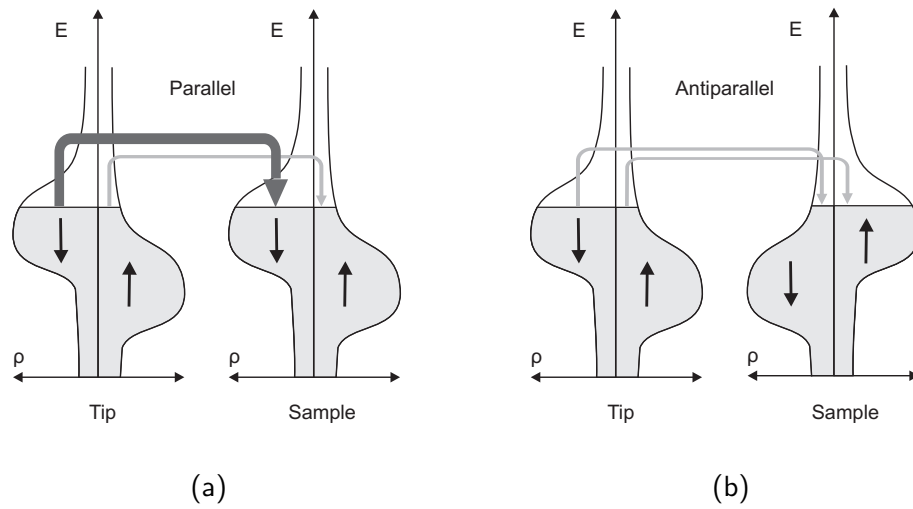


**Figure 2.8:** Stoner model of spin-polarized tunneling between two magnetic electrodes that exhibit (a) parallel and (b) antiparallel magnetization. In case of elastic electron tunneling the spin state is conserved during tunneling; spin-up electrons that tunnel out of the occupied states of the tip can only enter empty spin-up states of the sample. In case of parallel magnetization the total tunnel current is higher than in the case of antiparallel magnetization where both spin channels are small.

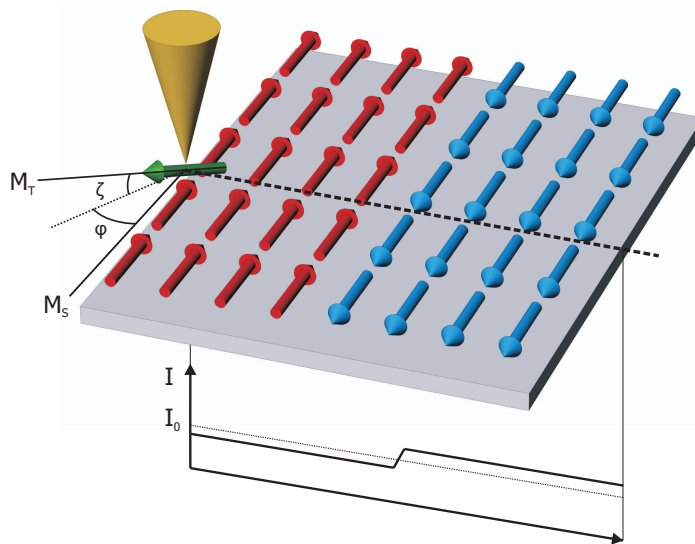


**Figure 2.9:** Schematic representation of an STM tip scanning over a magnetic domain wall and the corresponding tunneling current. The contrast in the tunneling current between the two magnetic domains depends on the angle between the magnetic quantization axis of sample and tip  $(M_T, M_S) = \cos(\theta) = \cos(\zeta) \cos(\varphi)$ .

One way to use the property of spin to measure the local magnetization of the surface below the tip is through direct measurement of the tunneling current. As can be seen from equation (2.29), the relative orientation of the quantization axis of both electrodes influences the strength of the tunneling current. This can be illustrated by the idealized model of a ferromagnetic domain wall that is imaged in constant current mode as schematically depicted in figure 2.9. When the tip is scanned over the dashed line the direction of the axis of magnetization of the sample will change sign at the domain wall causing a step in the measured value of the total tunnel current. A maximal contrast between the two magnetic domains is attained in case the magnetic axis of the tip  $\vec{M}_T$  is aligned parallel to the magnetic axis of the sample  $\vec{M}_S$ .

As mentioned in section (2.2.1) an STM that is being operated in constant current mode is only sensitive to the energy integrated LDOS of the sample. In addition, an SP-STM is also sensitive to the energy integrated local magnetization DOS of the sample, as can be seen from equation (2.27). However, the energy integrated LDOS of the sample  $\tilde{\rho}_S$  always increases with the bias voltage  $V$  whereas the energy integrated local magnetization DOS of the sample  $\vec{m}_S$  may stay constant or even change sign. For this reason, the non-spin-polarized tunneling current  $I_0$  is higher than the spin-polarized tunneling current  $I_{sp}$  and will thus dominate the total tunneling current, making a direct observation of the magnetic contribution difficult. In light of this fundamental obstacle, the model presented in figure 2.9 can be regarded as highly idealized and under most conditions it will be impossible to directly observe the magnetic corrugation from the tunneling current [35]. Although it is shown that it is possible to reveal complex atomic-scale spin structures with ultimate magnetic resolution in constant current mode SP-STM [32], it is unlikely that magnetic imaging of the domains of ferromagnetic surfaces by constant current mode SP-STM will play a major role in the future.

A way to overcome the limitations of constant current mode SP-STM and in the process separate the topographic, electronic, and magnetic information is the operation of an STM in spectroscopic mode, see section (2.2.2). Differentiation of equation (2.27) with respect to the voltage  $V$  yields a conductance of [32]:

$$\frac{dI}{dV}(\vec{r}_T, V, \theta) \propto \rho_T \rho_S(\vec{r}_T, E_F + eV) + \vec{m}_T \vec{m}_S(\vec{r}_T, E_F + eV). \quad (2.30)$$

A comparison of equation (2.30) with equation (2.27) reveals the essential difference between the contrast mechanisms of the two modes of operation. The constant current image is governed by the energy integrated quantities  $\tilde{\rho}_S$  and  $\vec{m}_S$ , whereas the differential conductivity is directly proportional to the LDOS  $\rho_S$  and local magnetization DOS  $\vec{m}_S$  of the sample at the energy  $E_F + eV$ . The bias voltage can be chosen to maximize the value of  $\vec{m}_S$  over  $\rho_S$ , thereby achieving maximum contrast. Analog to equation (2.29), equation (2.30) can by means of the definition of the polarization be rewritten in a somewhat more

user friendly form as [33, 34]:

$$\frac{dI}{dV}(\vec{r}_T, V, \theta) \propto \rho_T \rho_S(\vec{r}_T, E_F + eV) [1 + \cos(\theta) P_T P_S(\vec{r}_T, E_F + eV)]. \quad (2.31)$$

## 2.4 STM-Induced luminescence

Briefly after the invention of scanning tunneling microscopy it was realized the STM tip can induce the emission of photons. If one would be able to detect and analyze the emitted photons, the extreme spatial resolution of an STM can be extended into the optical domain. In 1988, Gimzewski *et al.* [36] published the first observation of light emission from an STM. Scanning tunneling microscope induced light emission (STM-LE) is potentially capable of correlating surface features with light emission induced by the tunneling current on an atomic scale.

### 2.4.1 Mechanisms of light emission

Electron or holes that are injected into a sample from the tip during the tunneling process can generate the emission of photons from the tunnel junction. Sakurai *et al.* [37] identified, depending upon the nature of the specimen probed, four fundamental mechanisms of light emission:

- Tip-induced excitation of surface plasmons in metallic surfaces. The in the metal injected electrons locally excite surface plasmons which subsequently may emit photons upon relaxation. The frequency of the emitted photons is approximately equal to the resonance frequency of the surface plasmon. The quantum efficiency of this process is  $\approx 1 \times 10^{-4}$  photons / injected electron.
- Electron-hole recombination in direct gap semiconducting surfaces. Minority carriers injected into a doped semiconductor recombine across the band gap with the readily available majority carriers, emitting photons with an energy equal to that of the band gap energy. The quantum efficiency of this process is  $\approx 1 \times 10^{-4}$  photons / injected electron. However, one should note that the process only results in a useful photon flux in case the injected carriers are minority carriers; if majority carries are injected, the small number of minority carriers available for recombination will be a limiting factor. A second limitation is that the total tunneling current, and thus the number of photons that are emitted, will be much smaller on a semiconductor in comparison to a metal.
- Direct dipole transitions in general materials, e.g. the Si(001) surface. Direct radiative transitions between the surface states of the tip and sample can occur in certain materials. The probability of this process to occur is relative small, with a quantum efficiency of  $\approx 1 \times 10^{-6}$  photons / injected electron.

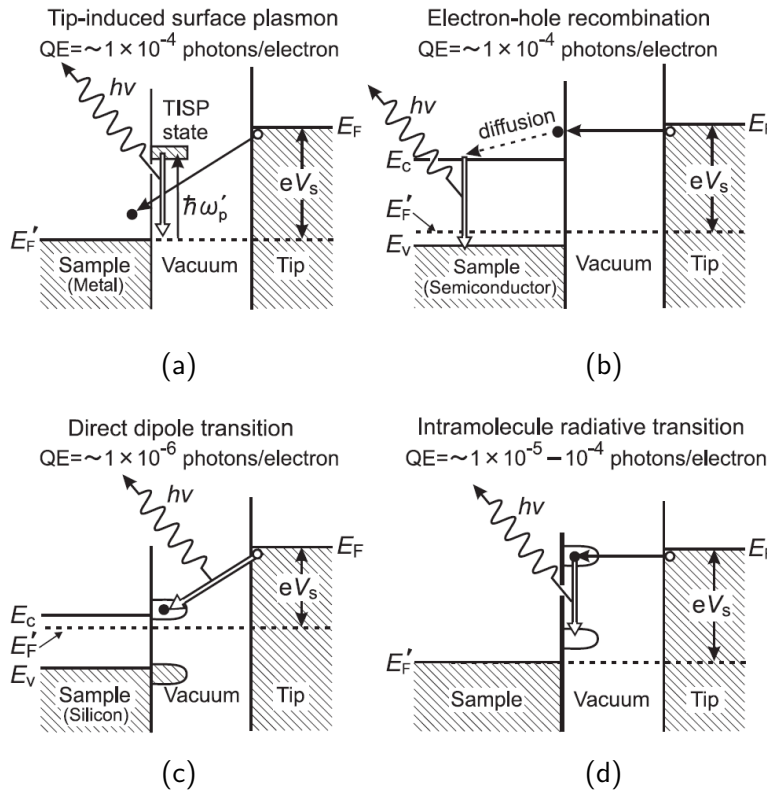


**Figure 2.10:** Schematic representation of the four mechanisms of STM-induced light emission [37]. (a) Nobel-metal surface. The plasmon mode is excited by the tunneling electrons to higher energy. The tip induced surface plasmon (TISP) decays radiatively. (b) III-V semiconductor surface. Photons with an energy equal to that of the band gap are emitted. (c) Si(001) surface. Dipole transition from the surface state of the tip to those of the sample provide light with an energy equal to the difference of the two energy levels. (d) Organic molecule adsorbed on the surface. Dipole transitions between the orbitals of the molecule produce light with an energy of the molecular level spacing.

- Intramolecular radiative transitions in organic molecules. Carriers from the tip can be directly injected into the molecular orbitals. Electronic transitions to a lower energy state within the molecule generate photons of energy equal to the molecular level spacing. The quantum efficiency of this process is  $\approx 1 \times 10^{-4} - 1 \times 10^{-5}$  photons/injected electron.

The four mechanisms of light emission are schematically illustrated in figure 2.10. In the light of the work done on the tungsten W(110) surface and of future research on semiconductors, only the first two mechanisms are of interest for the current study.

### 2.4.2 Resolution limit

As mentioned above, the primary benefit of STM-LE over other luminescence probe approaches is the extreme spatial resolution. that can be achieved by this technique. The spatial resolution of STM-LE is determined by three primary factors:

- STM tip radius. The size and shape of the apex of an STM tip determines the diameter of the “beam” of tunneling electrons. Since luminescence will primarily originate from within the region that is directly illuminated by the tunneling electrons, a sharper tip which results in a more narrow electron beam will subsequently result in more localized luminescence. As atomic resolution is routinely achieved in STM, indicating that the electron beam is, as explained in section (2.1.3), in the angstrom range, a similar resolution can be expected in STM-LE.
- Diffusion of the injected carriers. The area of the luminescent region will be determined by the length scale over which the injected carriers can diffuse before recombining. In contrast to other injection approaches, a tunneling electron beam is due to the low-injection energies of the carriers, typical 0–5 eV, a suitable means of inducing luminescence on a nanometer scale; the low injection energy will miniaturize the excitation regions or generation volumes [38, 39].
- Drift limitations of the STM. Due to low quantum efficiencies of the tunneling luminescence process of typically  $\approx 10^{-4}$  photons / injected carriers, long acquisition times are required to achieve a reasonable signal to noise ratio. Thermal drifting of the sample during the acquisition time will limit the resolution that can be achieved. In order to reduce the drift to a minimum and attain maximum resolution, STM-LE measurements should be preformed a ultra low temperatures.

In recent years, STM-LE with sub- and nanometer spatial resolution has been achieved at metal [40, 41], semiconductor [42–44], and absorbate covered surfaces [45, 46].

### 2.4.3 Imaging of magnetic structures

In the 1990s, it was reported that the by a STM tip induced photons emitted from a tunnel junction that included a ferromagnetic material had an unexpected circular polarization [47, 48]. As it turned out, the degree of circular polarization of the emitted photons could be related to the direction of the magnetization of the sample. Thus measurement of the polarization the STM-induced luminescence introduces the ability to probe magnetic materials with nanometer resolution; the spin polarization of the electrons tunneling from a ferromagnet can be determined by means of the degree of circular polarization

of the luminescence [49]. That this is experimentally feasible has been demonstrated in the case of electrons tunneling from magnetic Ni [50] and Fe [51] tips into III-V semiconductors and in case of tunneling from a W tip into a Co(100) surface [48].



## Chapter 3

# Planned experiment

A sample system that exhibits interesting magnetic properties is a tungsten W(110) surface covered with a thin film of iron (Fe). The magnetic properties of this sample have been intensively studied, e.g. [52–56]. As it turned out, the magnetic properties of such a sample system are ideal for demonstrating and characterizing spin-polarized tunneling. In this chapter the magnetic properties of the Fe/W(110) surface are examined and the outline of the experiment that was chosen to demonstrate the upgrade from a conventional STM to an SP-STM is given.

The sample-tip system under investigation in the current study consists of a slightly miscut W(110) crystal covered with 1–2 monolayers (ML) of Fe. The slight miscut results in flat terraces of approximately 7 nm wide. The thin layer of Fe was grown on the W(110) surface at room temperature and subsequently annealed to a substrate temperature of approximately 550 K. The post annealing of the substrate leads to so-called step flow growth in which, due to the high mobility of the Fe adatoms, the formation of critical nuclei on the middle of the terrace is avoided. Instead, the Fe adatoms settle on the step edges which are the adsorption sites that are energetically the most favorable. At coverages below 1 ML, the Fe will grow pseudomorphically on the W(110) surface [57], resulting in the surface being decorated with parallel monolayers of Fe which can be considered as nanowires. Upon completion of the first Fe layer, nanowires with a thickness of 2 ML begin to grow resulting in the sample surface being covered with alternating mono/doublelayer Fe nanowires, see figure 3.1a.

Well documented measurements on this particular sample system were done by [16]. In contrast to these measurements, the current investigation uses an Fe coated tungsten tip instead of a gadolinium (Gd) coated tungsten tip. An Fe coated tip differs from a Gd coated tip with respect to the orientation of its magnetic axis; an Fe coated tip will exhibit an in-plane magnetization axis, see section (7.3), whereas a Gd coated tip are expected to have an out-of-plane magnetization axis. Although the difference in tips will result in different  $dI/dV$ -spectra and contrasts, the measurements done on the sample system



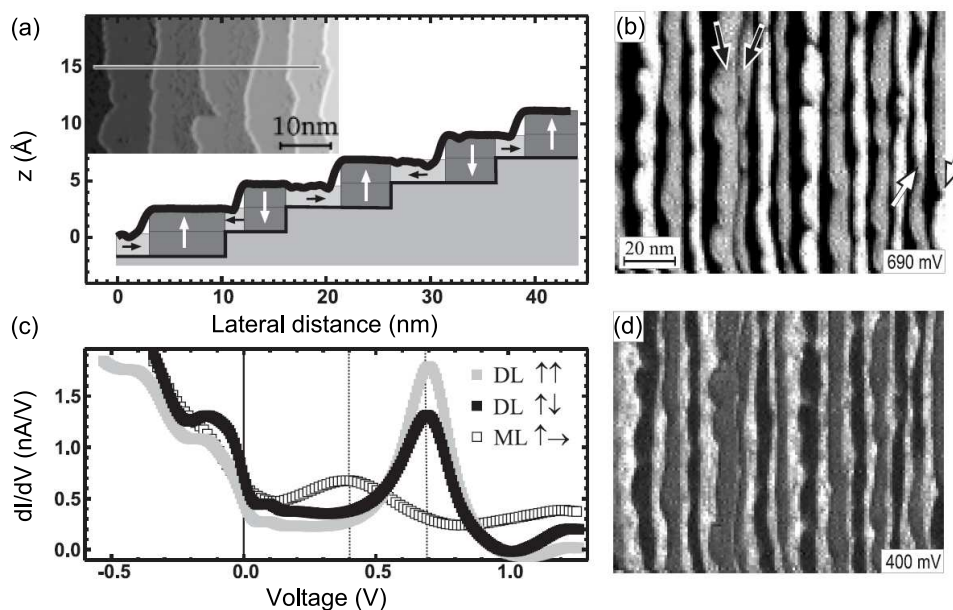


**Figure 3.1:** 1.5 ML of Fe on a slightly miscut W(110) crystal as measured by [16]. (a) Step flow growth results in alternating double- and monolayer nanowires. (b) With a Gd coated tip, three distinct  $dI/dV$ -spectra can be distinguished. (c)  $dI/dV$ -map of the surface at a voltage of 690 mV. The monolayer nanowires are dark whereas the doublelayer nanowires are respectively white and gray for parallel and anti-parallel magnetization. (d) A shift in contrast is observed when a voltage of 400 mV is applied; the monolayer nanowires are now bright.

with a Gd tip as performed by [16] will be explained below in more detail to further illustrate the concept of spin-polarized tunneling and gain more insight in the planned experiment.

The results of spin-polarized measurements on a Fe covered tungsten W(110) surface with a Gd covered tip as obtained by [16] are summarized in figure 3.1. In figure 3.1a, a cross section of a topographic image (inset) of a W(110) crystal covered with approximately 1.5 ML of Fe is shown. As can be seen, the Fe film has been grown in step flow mode which results in alternating double- and monolayer Fe nanowires. The double- and monolayer nanowires can be distinguished by  $I-V$  spectroscopy as can be seen in figure 3.1b which shows three distinct spectra. Since the measurements were done with a Gd coated tungsten tip of which it is known that it will possess an out-of-plane magnetization axis, see section (7.3), it can be deduced from the  $I-V$  spectroscopy that the doublelayer nanowires exhibit a magnetic axis that lies out-of-plane, whereas the magnetic axis of the monolayer nanowires lies in-plane. The highest difference between the three spectra is obtained at a bias voltage of 690 mV. At this voltage the white parts of figure 3.1c represent the doublelayer nanowires

---

of Fe that have their magnetic axis parallel to the magnetic axis of the tip. The gray areas also represent doublelayer nanowires, but with the difference that in this case the magnetic axis is anti-parallel to that of the tip. The third contrast is formed by the dark areas which represent the monolayer Fe nanowires which have an in-plane magnetization. Since the magnetic axis of the tip is out-of-plane, all the monolayer Fe nanowires look the same regardless the direction of their magnetic axis. Consequently, there is noway of determining the direction of the magnetic axis of the monolayer nanowires with a Gd coated tip. Figure 3.1d clearly demonstrates that in case the bias voltage is changed from 690 mV to 400 mV the contrast flips as predicted by the spectra of figure 3.1b.

The high contrast in the  $dI/dV$  images between areas with different direction of magnetization make this an ideal experiment to demonstrate spin-polarized tunneling in an STM. In light of this, the aim of the current report is the replication of this experiment, with the difference that the Gd coated tungsten tip is substituted for a Fe coated tungsten tip, to demonstrate that an in house STM can be upgraded to an SP-STM. To achieve this goal several "building blocks" are required. The first building block is obviously a scanning tunneling microscope. The STM that will undergo the upgrade to an SP-STM is the in house Omicron low temperature. The low temperature capabilities of this STM are required to lower the temperature below the Curie temperature,  $T_c=225$  K [58], of the monolayer nanowires.

In chapter 4, this STM is examined in detail. The second building block is the ability to deposit controlled quantities of ferromagnetic material on both the W(110) surface and the tips. Chapter 5 deals with this issue. The third building block of the planned experiment is attaining a W(110) crystal with a clean surface. To thoroughly clean the W(110) surface a high temperature oven has been designed and build in house. In chapter 6, the high temperature oven and the cleaning procedure that has been developed is presented. The fourth and final building block consists of magnetic tips. The preparation of such tips is addressed in chapter 7.



## Chapter 4

# Scanning tunneling microscope

The STM that is being upgraded to an SP-STM will be described in detail in this chapter. The STM in question is a commercially available Omicron low temperature STM and is schematically depicted in figure 4.1. This figure shows the STM without its additions such as: the high temperature oven, the evaporators, the vertical manipulator and the sputter gun. The most prominent feature in the figure is the big upright standing vacuum vessel that houses: the actual STM, an ion getter pump, a pressure meter, titanium evaporators, a carousel with six slots for storage of sampled and tips, and a cryostat that can be used to cool the STM to low temperatures.

Cooling of the STM to low temperatures is, due to reduction of thermal broadening of the local density of states, key to enhancement of spectroscopic details. In addition, cooling of the STM results in the inherent advantages of reduced surface mobility and minimized thermal drift. Furthermore, cooling below a sample's Curie temperature is required if one wants to study its magnetic properties. For these purposes the STM is equipped with a cryostat that consists of two separate compartments; an outer compartment that can be filled with liquid nitrogen and an inner compartment that can be filled with either liquid nitrogen or liquid helium. In case both compartments are filled with liquid helium the STM can be operated at a temperature of 77 K, while a operating temperature of 5 K can be reached in case the inner compartment is filled with liquid helium instead of liquid nitrogen.

In order to maintain UHV-conditions in the STM compartment, the compartment is equipped with an ion getter pump, which is a vacuum pump that works by ionizing the residual gases in the vacuum so that they can be adsorbed on a titanium layer on the walls of the pump. Because an ion getter pump does not have any moving parts it can, in contrast to a rotary turbo pump, be used during measurements. However, an ion getter pump can only be operated below pressures of  $1 \times 10^{-5}$  mbar and a turbo pump will still be needed to achieve this pressure. To further lower the pressure, both the STM compartment and the preparation compartment are equipped with titanium evaporators with which

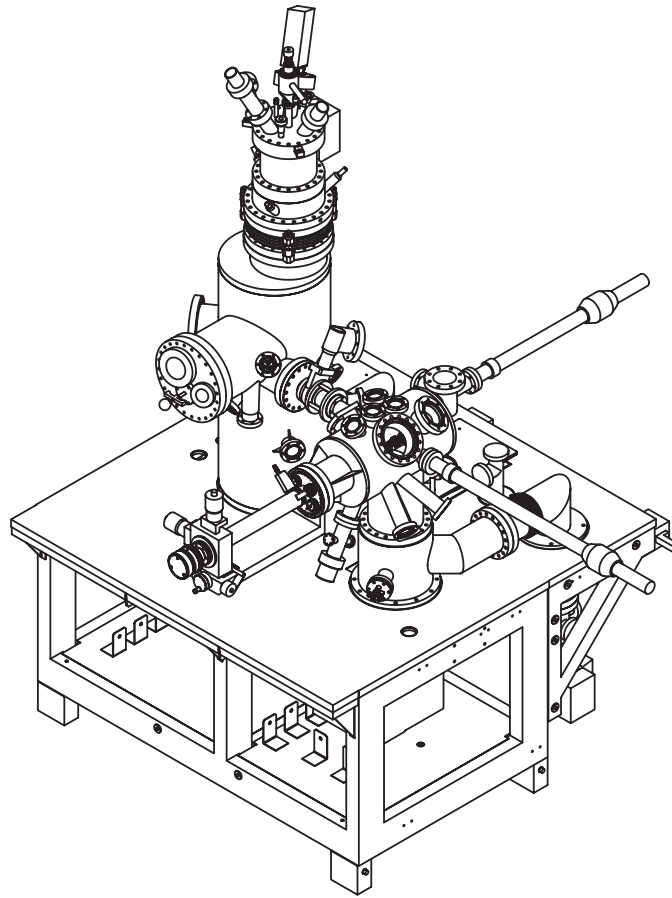


**Figure 4.1:** Drawing of the Omicron low temperature STM. Although not shown the evaporators, the developed high temperature oven, the sputter gun, and the vertical manipulator can be mounted on ports in the preparation chamber.

a thin layer of titanium can be deposited on the walls of the compartment. The titanium layer has a high sticking coefficient and will thus trap residual molecules or atoms on its surface.

The preparation compartment, so-called because in this compartment preparation of the tips and sample takes place, is also equipped with an ion getter pump. In addition it is, by a closable valve, directly connected to a turbo pump. In figure 4.1, it can be seen that the preparation compartment is equipped with a horizontal manipulator that can be used to move samples and tips to and from the STM compartment. In addition this manipulator is used to move around the samples and tips to and from the various positions in the preparation compartment where they undergo preparation. In the preparation chamber samples and tips can be stored under UHV-conditions, the W(110) crystal can be cleaned in the high temperature oven, thin layers of film can be deposited by the evaporators, and tips can be prepared.

For the purpose of tip preparation the preparation compartment is equipped with an oven capable of heating the tip and its holder to approximately 1200 K, an apparatus for separately glowing the tip up to approximately 1700 K installed on a vertical manipulator, and an argon sputter gun for additional cleaning of the tips. In addition an apparatus with which the field emission of the tip, and thus the geometry of the tip itself, can be characterized is installed on the vertical manipulator in the preparation compartment. This vertical manipulator is also equipped with three "parking lots" in which samples and tips can be stored.

The high temperature oven developed for cleaning the W(110) crystal is installed on a top side port (not shown in figure 4.1) in such a way that it can be retracted and thus does not hinder transport to and from the STM. In the original Omicron design a place for the three evaporators is allocated on three ports on the bottom/side of the preparation chamber. Due to the extreme positions through which the sample has to be maneuvered, which frequently resulted in the sample falling out of the slot, the evaporator (not shown in figure 4.1) that required the most extreme maneuvering of the sample was moved to a topside port.

The preparation compartment is, by means of a closable valve, connected to the load-lock compartment. The load-lock compartment can be separately pumped by the turbo pump and allows for loading and unloading of samples and tips into and out of the preparation compartment.



## Chapter 5

# Thin film depositing

As mentioned in chapter 3, the first step toward the realization of spin polarized tunneling is achieving the ability to deposit controlled quantities of ferromagnetic material on both sample and tip. For this purpose the Omicron LT-STM system is equipped with three Omicron EFM3 evaporators. At this time, only two of these evaporators are used in order to deposit ferromagnetic layers of iron (Fe) and chromium (Cr) on samples and tips. The method of calibration of these evaporators is explained in detail in the following section.

### 5.1 Evaporator calibration

To have control over the rate of deposition of ferromagnetic material these two evaporators have to be calibrated. In figure 5.1, the approach of calibration is schematically depicted. Two glass plates are clamped in a for this purpose specially developed sample holder in such a way that the top plate partially covers the bottom plate. Subsequently, the ferromagnetic material is deposited on top of the sample holder under ultra high vacuum (UHV) conditions. During the deposition, the flux of ferromagnetic material, measured by an in the evaporator integrated flux gauge, is kept constant over a specified time interval by means of a human feedback loop. The particle flux measured by the flux gauge is a measure of the number of charged particles in the total particle flux. One should note, that the ratio of charge particles to the total particles can and most likely will be different in case of different evaporant materials. After an deposit cycle, the top glass plate is removed under ambient conditions, leaving a ferromagnetic Heaviside profile on the bottom plate. This step profile of ferromagnetic material is subsequently investigated by means of an atomic force microscope (AFM).

In figure 5.2, an AFM image of a typical Heaviside profile of ferromagnetic material, in this case Fe, is depicted. From a large quantity of such images it proofed possible to extract a height profile as function of distance from the center of the deposited spot of ferromagnetic material, see figure 5.3. As can



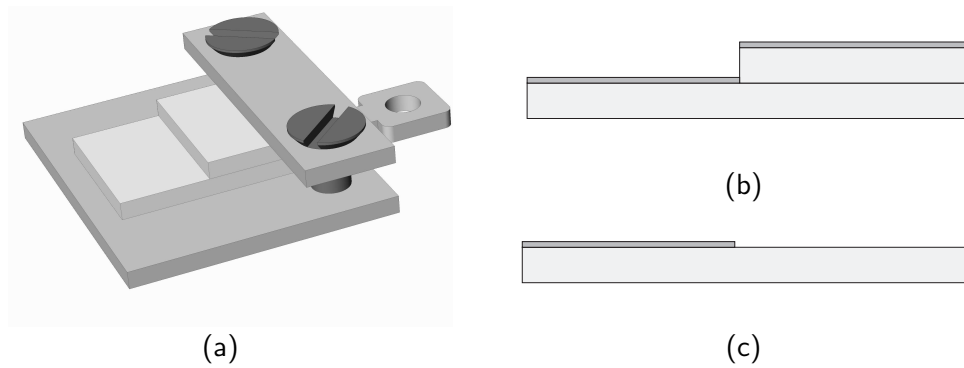


**Figure 5.1:** Principle of evaporator calibration. (a) Schematic representation of the for this purpose specially developed sample holder with two clamped glass plates. (b) Side view of the two glass plates after deposition of the ferromagnetic material (dark gray layers). (c) The Heaviside profile of ferromagnetic material left on the bottom glass plate after removal of the top glass plate.

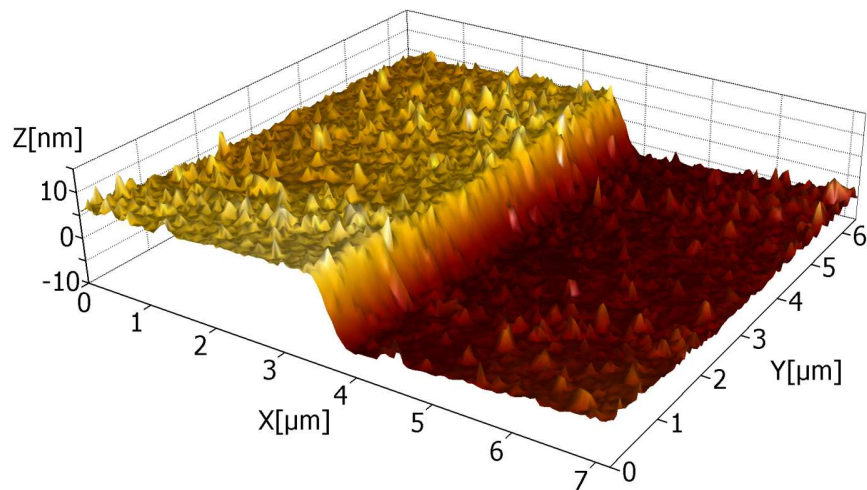


**Figure 5.2:** A typical Heaviside profile of ferromagnetic material left on the bottom glass plate measured with an AFM under ambient conditions.

be seen the spot was found to have a broad flat top, approximately 70 nm, and steep edges at its outer radius, which is ideal for depositing controlled quantities of ferromagnetic material on a sample or tip. The spot profile found is in excellent agreement with the in the EFM3 evaporator manual [59] specified spot profile.

In order to determine the rate of evaporation of the evaporators used the step height of the deposited ferromagnetic material has been determined for several times of depositing. The result of these measurements are presented in figure 5.4, which shows the step height of Fe and Cr in monolayers (ML) as a function of the depositing time. The Fe evaporator proved to have a deposit rate of  $0.74 \text{ ML min}^{-1}$  at a flux of  $10.5 \text{ nA}$  whereas the Cr evaporator has a deposit rate of  $0.30 \text{ ML min}^{-1}$  at a flux of  $100 \text{ nA}$  as measured by the flux gauge. This result clearly illustrates that the ratio of charged particles to the total particles is different for Fe and Cr; the Cr evaporant produces a particle flux in which the ratio of charged particles to the total particles is approximately 25 times higher than in the case of Fe. In table 5.1 the calibration settings, the dimensions of the evaporation rods, and the deposit rates are given for both the Fe and Cr evaporator.

During the calibration of the Cr evaporator it was found that an oxygen pressure of approximately  $5 \times 10^{-7} \text{ mbar}$  in combination with elevated temperatures will result in the formation of an chromium oxide layer. This chromium oxide layer subsequently results in an erratic behavior of the produced particle flux. Therefore, great care has to be taken to ensure that the evaporators are not used in an oxygen atmosphere. Since an oxygen atmosphere is required during operation of the high temperature oven, section (6.3), the evaporates should be cooled in order to prevent elevated temperatures in the evaporator and thereby the formation of oxide layers. Furthermore, it was observed that although the Cr evaporation rod has similar dimensions as the Fe evaporation rod it is much faster evaporated in totality. The calibration method above found that the evaporated material is not being deposited on the sample, or at least is not sticking to the sample. Further investigation is needed to shed some light on this observation. Since for the planned experiment only the Fe evaporator is needed, this is not done within the time frame of the current thesis.

**Table 5.1:** Overview of the calibration parameters of the evaporators: the dimensions of the evaporation rods, the particle flux at which the evaporator is calibrated, and the obtained deposit rates in monolayers per minute.

Evaporator	Shape	Thickness (mm)	Flux (nA)	Deposit rate ( $\text{ML min}^{-1}$ )
Fe	circular	2	10.5	0.74
Cr	square	2	100	0.30

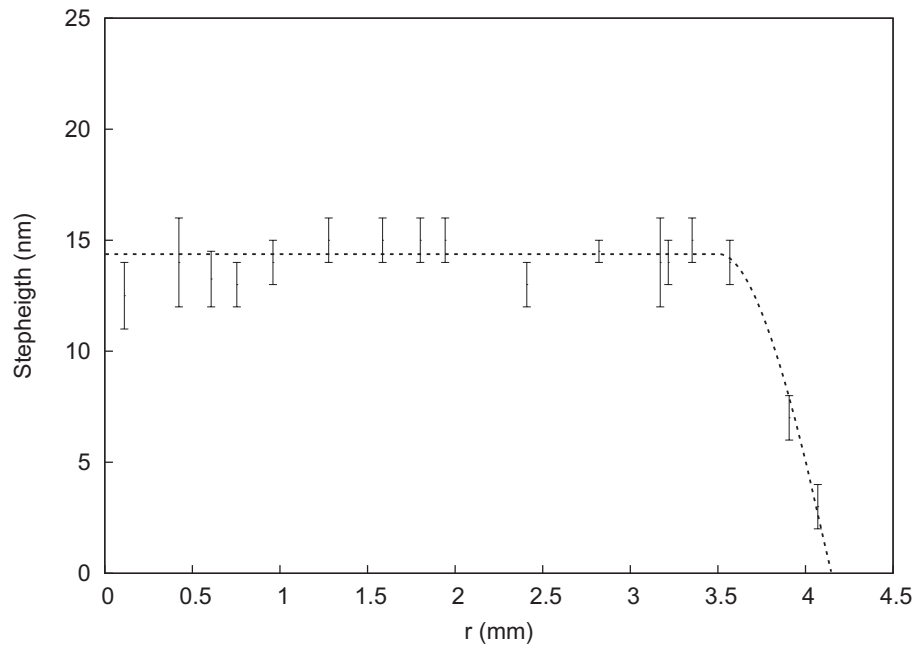


**Figure 5.3:** Height of a typical spot of deposited ferromagnetic material (Fe) as a function of distance from the center. The spot has a broad flat top with a diameter of  $\approx 70$  mm. At the edges of the spot, the height of deposited ferromagnetic material as a function of the radius falls off steeply.

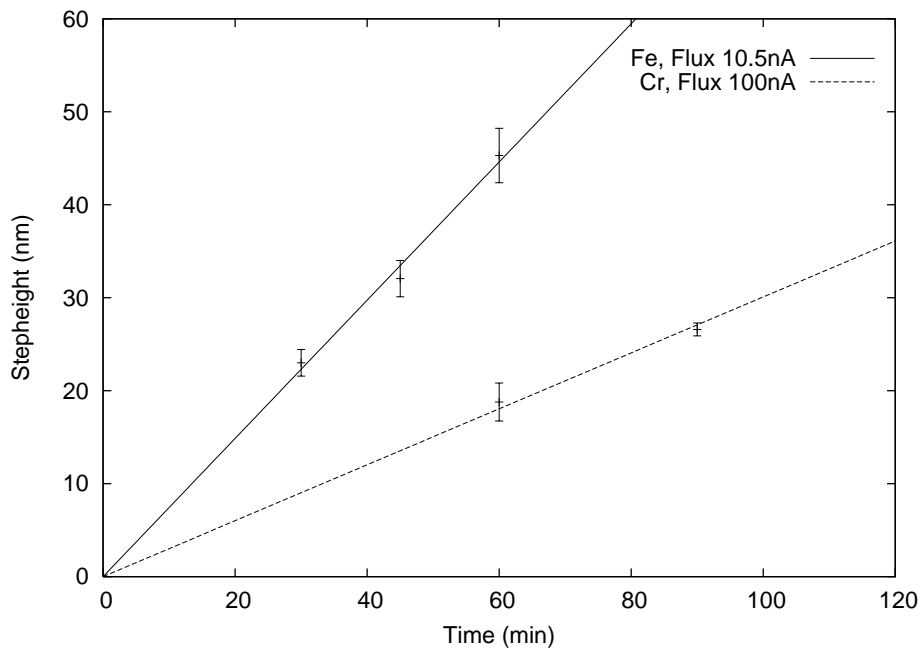


**Figure 5.4:** Measured step height and the standard deviation (vertical bars) in monolayers as a function of depositing time for Fe and Cr.

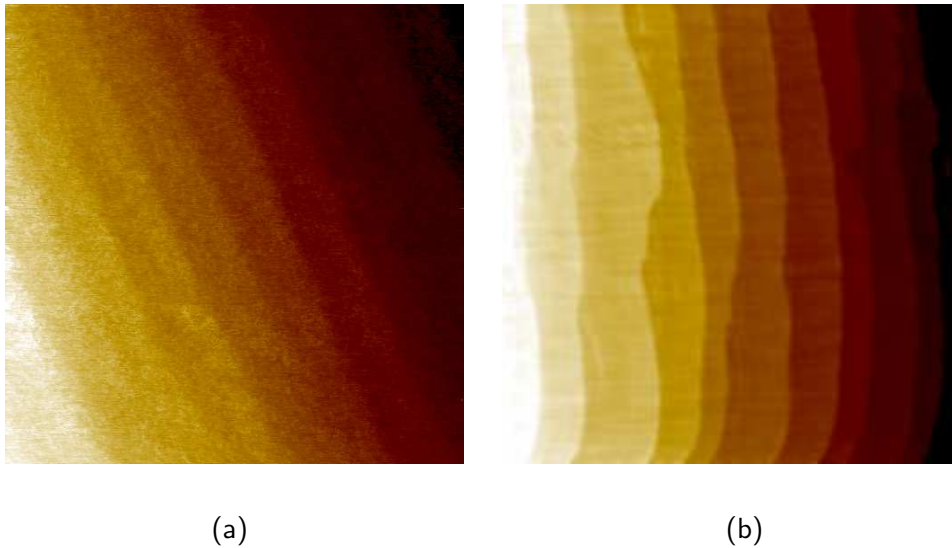


**Figure 5.5:** 80×80 nm STM images of Fe grown on the W(110) surface. (a)  $\approx 0.5$  ML Fe grown at room temperature. Individual islands of Fe can be seen, indicating that step flow growth did not take place. (b)  $\approx 1.5$  ML Fe grown on the W(110) surface with post annealing of the sample to 550 K for 4 minutes. No individual Fe islands are visible indicating that step flow growth did take place.

## 5.2 Step flow growth

As explained in chapter 3, the planned experiment requires step flow growth of Fe on the W(110) surface. Such growth can be achieved by growing the Fe film at room temperature and subsequently post annealing of the W(110) surface to a temperature of approximately 550 K for 4 minutes [60]. In figure 5.5(a), an STM measurement performed on a by  $\approx 0.5$  ML Fe covered W(110) surface grown at room temperature is shown. Individual islands of Fe can be seen, indicating that step flow growth did not take place. In figure 5.5b, an STM measurement performed on a by  $\approx 1.5$  ML Fe covered W(110) surface which has been post annealed to approximately 550 K for 4 minutes is shown. As can be seen, there are no individual Fe islands on the surface from which it can be concluded that step flow growth did indeed take place.



## Chapter 6

# High temperature oven

In order to clean the W(110) surface on which the thin film of Fe will be deposited a high temperature oven capable of sustained heating of the W(110) crystal up to  $\approx 1700$  K and flashing up to  $\approx 2500$  K was designed, build and tested in house. In figure 6.1, the final design of the high temperature oven is depicted.

### 6.1 Materials

As can be seen in the explosion view of figure 6.1b, the high temperature oven consists of numerous parts of which most are made out of materials chosen for their high melting point. First of all, the white spacers which electrically isolate the different parts of the oven, are made out of aluminum oxide ( $\text{Al}_2\text{O}_3$ ) that has a melting point of  $\approx 2300$  K. The spacers were ordered from a specialized firm [61] and did in their original form not fit into the design of the high temperature oven. The required alternations to the spacers where done by application of a diamond drill. Since  $\text{Al}_2\text{O}_3$  is an extremely hard material, this proofed to be very time consuming and painstakingly work.

The sample holder and the bolts that run through the entire oven and thereby form the backbone of the oven are made out of molybdenum, which has a melting point of  $\approx 2900$  K. Since molybdenum is a hard material and consequently difficult to manipulate, these molybdenum parts were ordered to be custom build by a specialized firm [62]. In order to avoid the bolts fusing together with the nuts at the elevated temperature that are reached in the oven, the material out of which the nuts where made was chosen to be tantalum, which has a melting point of  $\approx 3300$  K. As in the case of the molybdenum bolts, the tantalum nuts were ordered to be custom made by a specialized firm [62]. In addition to the tantalum nuts, the tantalum heat shielding was also custom made.

The last part that needed to be custom made [63] was the sapphire block through which the molybdenum and stainless steel bolts run. Sapphire was

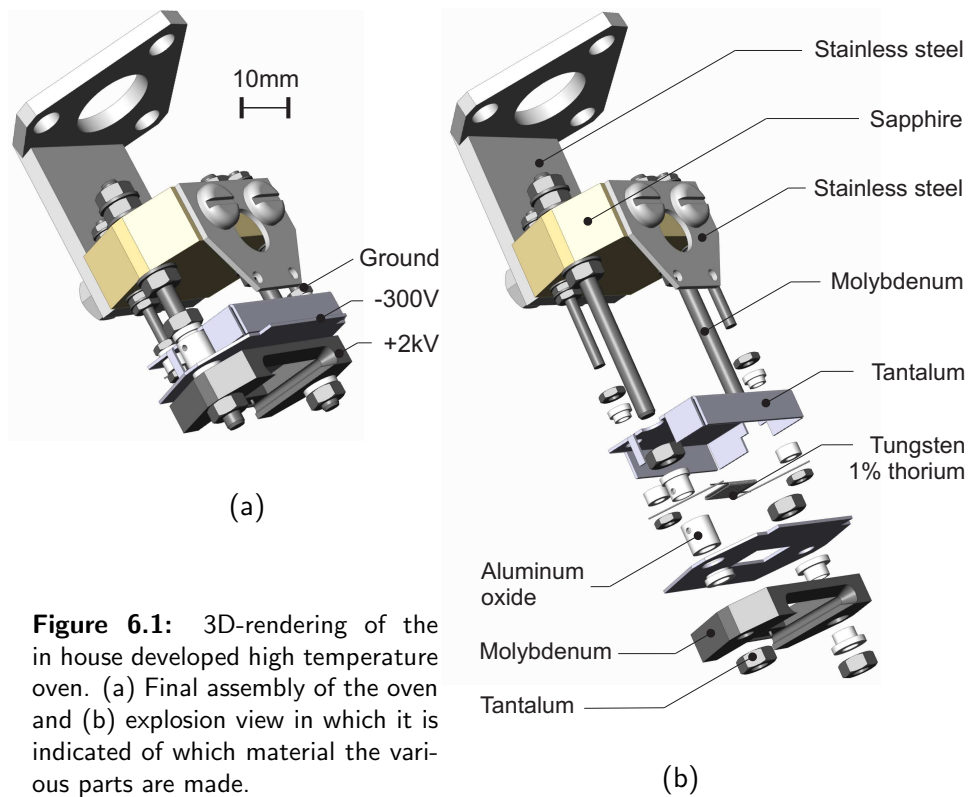


**Figure 6.1:** 3D-rendering of the in house developed high temperature oven. (a) Final assembly of the oven and (b) explosion view in which it is indicated of which material the various parts are made.

chosen as a material for this part because it is an electrical isolator and has a melting point of  $\approx 2300$  K. The remainder of the parts were all made in the in house workshop. To conclude the material review; the filament was made out of a tungsten wire with an 1% thorium contamination instead of a pure tungsten wire. The thorium dopants lower the work function of the tungsten resulting in an increase in the number of electrons emitted.

## 6.2 Operational principle

The developed high temperature oven can be classified as an electron-beam heater; electrons, generated by directing a current through a filament, are forced by a high electric field to the sample on which they impact with high energy thereby heating the sample.

The high electrical field that drives the electrons from the filament to the sample and sample holder is generated by application of a high potential, in this case +2 kV, to the sample holder. Electrically isolating the sample holder from the rest of the high temperature oven proved to be a daunting task. First of all, to maximize the number of electrons that impact on the sample, the design of the high temperature oven called for a minimalization of the distance between filament and sample. Since this leaves no room for elaborate constructions

that reliably electrically isolate the various parts of the oven, only thin isolating spacers were used. Due to thermal expansion of the various parts and the fact that they are in very close proximity to each other, it proved difficult to avoid spark overs. Secondly, the addition of a triode to the design of the high temperature oven introduced an other element that has to be electrically isolated from the other parts. The triode consists of a tantalum plate in which a square hole is cut. By application of a negative potential to this plate, in this case  $-300\text{ V}$ , the electron beam that is directed to the sample and sample holder is squeezed resulting in the electrons being focused on the sample thereby more locally heating the sample instead of the sample holder. Although it was a daunting and by times frustrating task, it proved possible to avoid spark overs by placing customized isolating spacers at the right spots.

A heat shield is placed above the filament in order to shield the top part of the oven where all the wire connections are. In order to maximize the number of electrons impacting on the sample, the high temperature oven was designed in such a way that the heat shield is in electrical contact with the triode plate, subsequently repelling the electrons and directing them to the hole of the triode plate.

With this high temperature oven design it proved to be possible to deposit  $400\text{ W}$  onto the sample thereby flashing it to  $\approx 2500\text{ K}$ , which can be considered as a remarkable feature since this power is transmitted in a free electron beam under ultra high vacuum conditions.

### 6.3 W(110) cleaning procedure

The surface of a tungsten single-crystal of standard purity is, even after mechanical and chemical polishing, covered with impurities which predominantly consist of carbon and oxygen [64]. The impurities are not restricted to the surface of the W(110) crystal, but are adsorbed into the bulk material [65, 66]. In order to remove these impurities from the W(110) crystal and obtain a clear surface the high temperature oven, described in detail in the previous sections, is employed.

The most effective method to remove the carbon contamination from the outermost layer and simultaneously deplete the surface region of carbon impurities is heating the tungsten crystal in an oxygen atmosphere [67, 68]. The oxygen present will react with the carbon adsorbed on the surface to form CO-species which, at high enough temperatures, will be evaporated. The removal of the carbon from the outermost layer results in carbon segregation to the surface where the carbon will oxidize to form CO and  $\text{CO}_2$  which are subsequently removed by evaporation. After this carbon depletion treatment there will still be oxygen present at the surface. This oxygen contamination can be removed by flashing the W(110) crystal under UHV-conditions to temperatures in excess of  $2500\text{ K}$ . Repetitive cleaning cycles of the carbon depletion treatment followed by oxygen



**Table 6.1:** Overview of the W(110) cleaning procedure. The cleaning procedure is divided into three stages. The first stage serves as a bakeout in case the oven has been exposed to ambient conditions. The second stage removes the worst carbon contaminants and is followed by a third stage that should be repeated several times to ensure that the W(110) crystal is as clean as possible.

Mode	Time	Pressure	Temp.	Input power
Continues <sup>1</sup>	one day	UHV		50 W <sup>5</sup>
Continues <sup>2</sup>	several hours	$1 \times 10^{-6}$ mbar O <sub>2</sub>	1500 K	120 W <sup>6</sup>
Flashing <sup>3</sup>	10 sec. 20–30×	UHV	2500 K	250 W <sup>6</sup>
Continues <sup>4</sup>	$\frac{1}{2}$ hour	$1 \times 10^{-7}$ mbar O <sub>2</sub>	1500 K	120 W <sup>6</sup>
Flashing <sup>4</sup>	10 sec. 20–30×	UHV	2500 K	250 W <sup>6</sup>

<sup>1</sup> The first stage serves as a bakeout in case the oven has been exposed to ambient conditions. This step can be done without a W(110) crystal inserted.

<sup>2</sup> Be mindful that in case of the pressure rising above approximately  $5 \times 10^{-6}$  mbar spark overs will frequently occur. When most carbon contaminants are removed the pressure should decrease slowly.

<sup>3</sup> When flashing the W(110) sample holder be careful not to let the pressure rise above  $5 \times 10^{-6}$  mbar in order to avoid spark overs. In case of good pressure the duration and wattage of the flashing can be increased.

<sup>4</sup> This stage should be repeated several times. After each cycle the pressure should show a decrease in comparison with the previous cycle, indicating that the cleanliness of the W(110) crystal is increased.

<sup>5</sup> Wattage of the filament.

<sup>6</sup> Wattage deposited on the W(110) sample holder.

removal are necessary to attain a clean W(110) surface. In table 6.3, an overview of the W(110) cleaning procedure is given. A more thorough description of the W(110) cleaning procedure can be found in the literature [64].

In figure 6.2, STM images of the W(110) surface accompanied by a characteristic  $I-V$  spectrum of the imaged surface are presented. As can be seen in figure 6.2a, sustained heating of the crystal up to  $T \approx 1000$  K yields a surface that is far from clean. In addition to big clumps of contaminants, single adsorbates are visible. The characteristic  $I-V$  spectrum spectrum for this image clearly shows a band gap, indicating the presence of an oxide layer. After sustained heating of the crystal up to  $T \approx 1700$  K the big clumps of contaminants are gone. However, the inset of figure 6.2b shows that there are still single adsorbates present. The characteristic  $I-V$  spectrum spectrum does not show a band gap as in the case of sustained heating up to  $T \approx 1000$  K, but instead

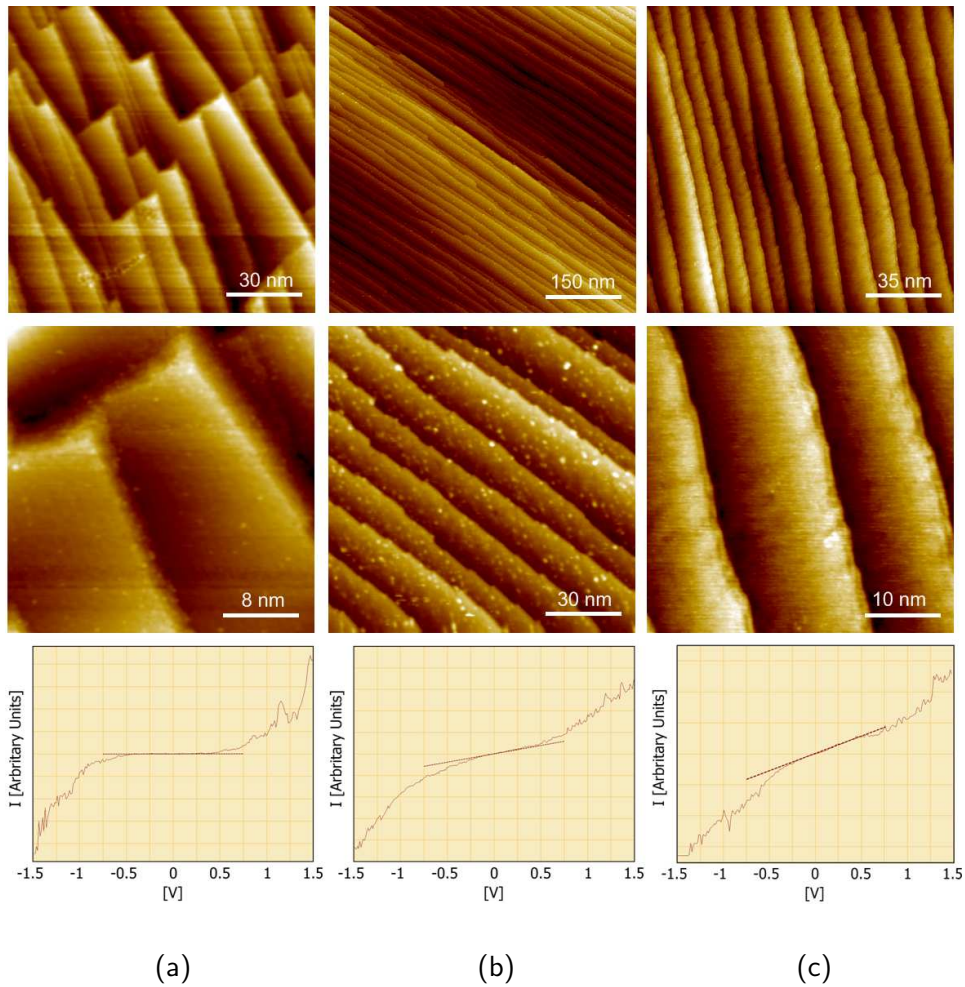


**Figure 6.2:** STM images of the W(110) surface and a characteristic  $I$ - $V$  spectrum at three different stages in the cleaning process. (a) Sustained heating up to  $T \approx 1000$  K. Big clumps of contaminations and single adsorbates are visible while the  $I$ - $V$  spectra show a band gap, indicating the presence of an oxide layer. (b) Sustained heating up to  $T \approx 1700$  K. Single adsorbates are still present on the surface. Some of the  $I$ - $V$  spectra show metallic behavior. (c) Repeated flashing up to  $T \approx 2500$  K. The surface is clean without any visible adsorbates and the  $I$ - $V$  spectra show metallic behavior for the entire surface.

shows metallic behavior. It should be noted that not all spots on the surface showed this metallic  $I$ - $V$  behavior, indicating that an oxide layer is still partially covering the surface. After the last step of the cleaning process, which consisted of flashing the sample up to  $T \approx 2500$  K, a clean surface W(110) is obtained. As can be seen in figure 6.2c and its inset, the single adsorbates are gone while the  $I$ - $V$  spectrum was found to show metallic behavior for all spots on the surface. 4



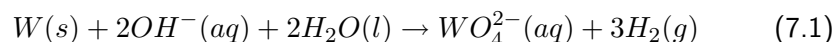
## Chapter 7

# Tip preparation

In order to reproducibly make a sharp non-spin sensitive STM-tip of high quality, an etching procedure, described by various authors e.g. [69–71], is used. This etching procedure, described in detail in section (7.1), is taken as the starting point for the creation of spin sensitive STM-tips. Upon successful completion of the etching procedure, the newly formed tips are introduced into the preparation-chamber of the Omicron LT-STM where they will undergo further preparation. After the *in situ* preparation steps, described in detail in section (7.2), the tips will be ready for use in conventional non-spin-polarized STM. In order to make the tips spin-sensitive and thus ready for use in spin-polarized STM, a small modification to the standard etching procedure is needed. Furthermore, thin layers of ferromagnetic material have to be evaporated on the tip to make it magnetic. These two processes are described in detail in section (7.3)

### 7.1 Etching

The tips are made of a 99.97% pure poly-crystalline tungsten (W) wire with a diameter of 0.25 mm. A short piece of this wire is fixated in a tip-holder in such a way that approximately 4 mm of the wire is extended. After a thorough cleaning of the tip-holder and the extended tungsten wire in an ultrasonic bath, the wire is etched in a 2.0 molar KOH solution. To this end, approximately 2 mm of the extended tungsten wire is submerged in the etchant. A positive voltage of 6.30 V is applied between the tip-wire and a platinum-iridium (90% / 10%) spiral that serves as a counter electrode, see figure 7.1. In the reaction that subsequently takes place:



the tungsten is dissolved. To ensure that the  $H_2(g)$  bubbles which are produced at the platinum-iridium anode do not disturb the etching process, the beaker-glass in which the etching is performed consists of two compartments that are partially separated by a vertical glass plate in the middle, see figure 7.1. After

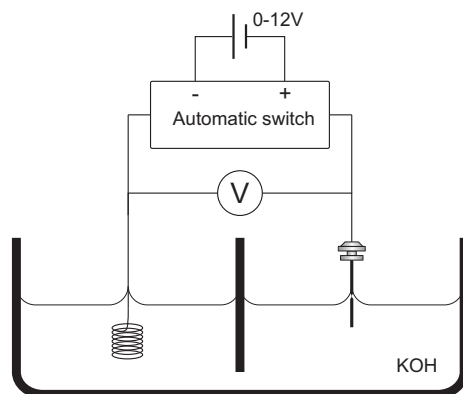
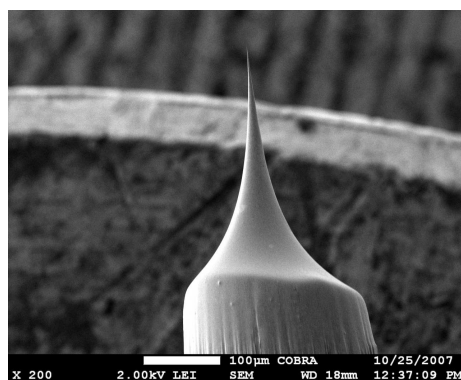
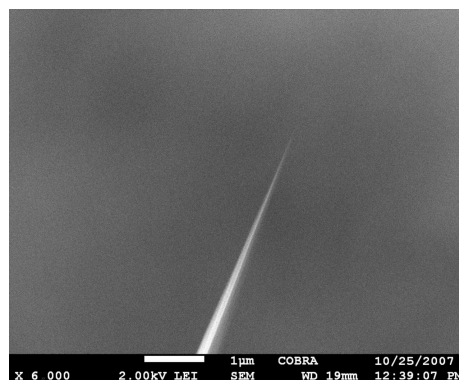


**Figure 7.1:** Schematic representation of the setup used for etching the tips. A positive voltage is applied to the tip holder and its extended tungsten wire. The submerged tungsten wire is separated by a vertical glass plate from a platinum-iridium spiral that serves as a counter electrode. As an etchant a 2.0 molar KOH solution is used. To ensure that after breakage of the tungsten wire the newly formed tip is not etched blunt, an automatic switch is.



(a)



(b)

**Figure 7.2:** Scanning electron microscope image of etched STM-tips. (a) Etched tip at 200× magnification. (b) 10000× magnification of the apex of the same tip. The diameter of the apex is found to be at least smaller than 100 nm.

the reaction products have dissolved into the etchant they sink down, a process that can be observed due the local change of the solution's refractive index along the reaction products' path. In case the tungsten wire is placed vertically in the etchant, the reaction products will sink down the wire and partially shield the wire from etching. At the point where the tungsten wire penetrates the surface of the etching solution a meniscus, which plays a key role in the etching procedure and is very sensitive to surface contaminations and vibrations, will form. At the meniscus the shielding of the tungsten wire by the already dissolved reaction products is lowest, resulting in the highest etching rate at this point. The high etching rate at the meniscus may cause a pulling of the meniscus and it's subsequent collapse during the final stage of etching. In order to avoid the collapse of the meniscus, the etching process is interrupted at approximately three quarters of the process. The tip is taken out and put back into the etching solution yielding a new meniscus that will remain stable to the end of the etching process. During the final stage of the etching process the tungsten wire will abruptly break at its thinnest place leaving a sharp tip that can be used in STM. To ensure that the newly formed tip is not etched blunt after breakage of the tungsten wire, a fast automatic switch terminates the voltage when the current falls below a preset threshold.

In figure 7.2, a scanning electron microscope (SEM) image of a tip that was prepared by the etching technique described above is depicted. As can be seen, the etching procedure results in a very sharp tip with an apex diameter that is smaller than 100 nm. After a quick inspection by means of a microscope to determine if the etching process was completed successfully, the tip is placed in a tip-holder and introduced into the preparation-chamber of the STM where it will be further sharpened and prepared for use.

## 7.2 In situ preparation

Once the freshly etched tips are introduced into the preparation chamber of the STM, the first performed action is heating the tip and its holder up to approximately 550 K. By baking the tip and its holder, possible contaminants such as water and organic sediments will evaporate and be pumped away. In this way, contamination of the STM chamber by a possibly dirty tip-holder can be reduced to a minimum.

After baking the tip and its holder, the oxide layer on the tip is removed by heating the tip separately. For this, the tip is brought in ohmic contact with a sharp conducting plate as schematically depicted in figure 7.3a. Since the contact between the two is a localized point contact with a relative high electrical resistance, directing a current through it will locally heat up the tip while the holder will remain at relative low temperature. The tip will glow orange, indicating that the temperature is about 1200–1400 K. At this temperature most of the oxide layer will be removed. In case a conventional non-spin sensitive tip

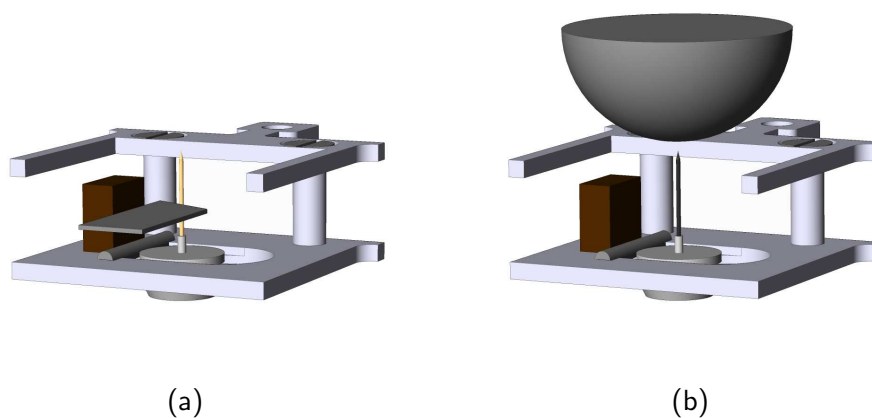


**Figure 7.3:** Schematic representation of two steps in tip preparation process. (a) Heating of the tip by directing a current through a point contact between a thin metal plate and the tip. (b) Characterization of the tip by means of field emission. Application of a high enough voltage between the half sphere and the tip will generate a current that is characteristic for the diameter of the tip's apex.

is pursued, the tip is kept at this temperature for approximately 20 minutes. In addition to removal of the bulk of the oxide layer on the tip, the tip is further sharpened by this treatment [69, 72, 73].

After the glowing of the tip, the tip is bombarded with argon ions ( $\text{Ar}^+$ ) for approximately 20 minutes. The argon bombardment further cleans and mechanically stabilizes the tip without changing its tip radius to much.

In order to get a good indication of the quality of the tip apex before loading the tip into the STM-chamber, the tip is brought in close proximity to a half steel sphere, see figure 7.3b, to which a positive voltage is applied. This will create a strong electric field around the apex of the tip. The high electric field will force electrons to be emitted from the apex, generating a current. The voltage necessary for creating this current, the so-called field emission voltage [73], is a measure of the radius of the tip apex; sharp tips will emit electrons at relative low applied voltages, whereas a tip with a round apex will require the application of a much higher voltage to achieve the same current. In the field emission setup of the Omicron low temperature STM, the distance between the half steel sphere and the tip cannot be controlled precisely. Therefore, only a qualitative indication of the sharpness of the tip can be obtained. Typically, 1 mA current will flow at an applied voltage of several hundreds volts. If the onset of the field emission is not found below an applied voltage of 2 kV, the tip is most likely broken or very blunt. Furthermore, if the emission current is fluctuating wildly, the tip is most likely to be very unstable. In both case the tip is discarded.

## 7.3 Magnetic tips

In order to gain magnetic sensitivity with the in house Omicron low temperature STM, or more generally in any STM, a magnetic tip is needed. A magnetic tip can be obtained in several ways. Obviously, the simplest approach is using bulk ferromagnetic tips. The problem encountered in this approach are the strong stray fields that are generated by the bulk ferromagnetic material. These stray fields give rise to dipolar interaction between the tip and sample, potentially modifying or destroying the sample's intrinsic domain structure. This problem can be solved by either using bulk anti-ferromagnetic tips or non-magnetic tips covered with a thin film of (anti)-ferromagnetic material [74]. The former approach has the advantage of a total absence of any macroscopic dipolar stray field. However, since the magnetization direction in bulk anti-ferromagnetic tips will be solely governed by the shape anisotropy of the tip, bulk anti-ferromagnetic tips do not allow for adjustment of their magnetization direction. Adjustment of the magnetization direction is possible if, instead of a bulk anti-ferromagnetic tip, a bulk non-magnetic tip that is covered with a thin magnetic film is used. In contrast to the bulk anti-ferromagnetic tips, the magnetization direction of the tip can be adjusted by an externally applied magnetic field or choosing an appropriate film material and thickness [16, 75]. For example, on a tungsten tip with an apex diameter in the order of  $1\ \mu\text{m}$ , the following magnetization directions are observed:

- 3–10 ML Fe, in-plane magnetization.
- 7–9 ML Gd, out-of-plane magnetization (sometimes in-plane).
- 10-15 ML  $\text{Gd}_{90}\text{Fe}_{10}$ , out-of-plane magnetization.
- 25-45 ML Cr, out-of-plane magnetization.

The fact that the direction of magnetization can differ for different film materials and thickness can, at least qualitatively, be understood. Two anisotropy terms have to be considered: the shape anisotropy which arises due to the pointed shape of the tip, and the surface and interface anisotropy of the thin film. The former will always try to force the magnetization along the tip axis whereas the latter is material and thickness dependent and can be tuned to either overcome or enhance the effect of the shape anisotropy. In case a tip with a relatively large apex is used, e.g.  $1\ \mu\text{m}$ , the influence of the surface and interface anisotropy of the thin film on the magnetization direction can be considered the same as that of an equivalent film on a flat substrate. Since a lot of investigation was done on the direction of magnetization of thin films on flat substrates, a suitable ferromagnetic material with which to cover the tip can be selected from literature. Another advantage of such blunt tips is that they greatly increase the change of successfully generating magnetic tips. It is reported in literature that in case sharp tips are used as the starting point for the creation of magnetic



tips, the magnetic material will be frequently lost during the approach [74]. Furthermore, such tip would not nearly exhibit the stability of blunt tips.

In the current study a tungsten tip covered with a thin film of 3–10 ML Fe is used to demonstrate spin-polarized tunneling. As in the experiment of [16], it is opted to use a tip that has an apex diameter of approximately  $1\ \mu\text{m}$ . The common approach to generate such blunt tips is by *in situ* heating of a sharp tips to 2200 K [74, 16, 76]. The heating of a tungsten tip to this temperature results in melting of its apex, which consequently results in an increase of its apex diameter to  $\approx 1\ \mu\text{m}$ . This procedure has the advantage that any adsorbates that maybe present on the tip, which typically reduce the spin-polarization and will have a negative influence on the signal-to-noise ratio, are removed from the tip leaving a clean surface on which the magnetic thin film can be deposited. Several ways of heating the tip up to 2200 K in the in house Omicron low temperature STM have been tried:

- Heating of the tip by directing a current through a ohmic point contact. This is the same approach which is normally used to clean sharp tips, as explained in section (7.2), but with a higher current. It was found that this approach frequently resulted in breakage of the tip at the point contact. Furthermore, SEM images of tips that did survive the heating process show that the tip is still sharp and melting of the apex did not take place, see figure 7.4a.
- Heating of the tip by use of field emission setup. In this approach the field emission setup, which is normally used to characterize the tip as explained in section (7.2), is used to generate a spark over between the tip and the half metal sphere. For a brief moment during the spark over, a high current will flow through the apex of the tip subsequently resulting in its melting. However, as can be seen in figure 7.4b, this procedure resulted in tips that are far to blunt for use in STM. Moreover, the result proofed not to be reproducible.
- Heating of the tip by use of the high temperature oven. In this approach the tip is inserted into the high temperature oven and subsequently heated. The problem encountered in this approach is that the tip could not be heated enough without melting of its holder. Furthermore, the magnets present on the tip-holder, essential for keeping the tip in its holder during transport, were heated above their Curie temperature and subsequently failed to function. In figure 7.4c, the apex of a tip of which its holder was molten is depicted. As can be seen the tip is still sharp and melting of the apex did not take place.

All these methods of *in situ* cleaning of the tip proofed to be unsuccessful. Therefore, the next best approach was used: etching a blunt tip with an apex diameter of  $\approx 500\ \text{nm}$  and subsequently *in situ* heating it to  $\approx 1700\ \text{K}$  by means

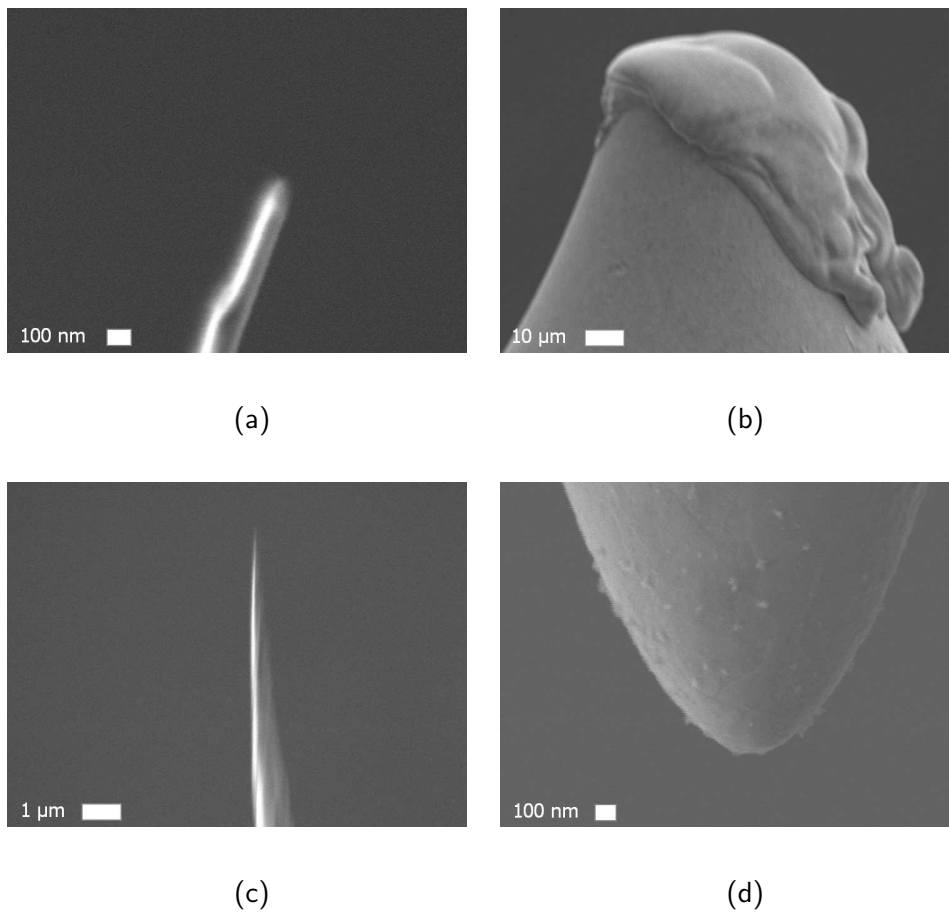


**Figure 7.4:** SEM images of the tip apex after various tip preparation procedures. (a) Glowing of the tip by means of a ohmic point contact. The diameter of the tip apex is found to be smaller than 25 nm. (b) Melted tip apex due to a spark over generated by the field emission setup. The tip apex is far to blunt for use in STM. (c) Heating of the tip in the high temperature oven. The maximum temperature of the tip that could be achieved was limited by the relatively low melting point of the tip-holder. The diameter of the tip apex is smaller than 100 nm. (d) Further etching after the drop off. The diameter of the tip apex is found to be approximately 500 nm.

of the point contact approach. In this way, the influence of the surface and interface anisotropy of the thin film will closely resemble those of thin films on tips with a melted apex. However, tips that are prepared in this way will probably suffer from some contaminations which may, as mentioned above, result in a reduction in spin-polarization and a lower signal-to-noise ratio.

To generate these blunt tip, the tips were first etched sharp conform the etching procedure described in section (7.1). After the drop off, the etching procedure was continued  $5\times$  for approximately half a second by means of manually applying the voltage. This reproducible yields tips with an apex diameter of  $\approx 500$  nm, as can be seen in figure 7.4d.

Upon successful completion of the etching process, the tip is put through the same *in situ* preparation steps as the sharp tips described in section (7.2), i.e. heating of the tip-holder, glowing of the tip, and an  $\text{Ar}^+$  bombardment. The second step, the glowing of the tip, is done with current settings that are as high as the integrity of the tip and especially the tip holder allows. In this way, the tip is heated to its maximum temperature and the number of contaminants present on the apex of the tip will be reduced to a minimum.

The final step in the preparation of the magnetic tips is the depositing of a thin ferromagnetic film. For initial measurements on the Fe/W(110) surface a 7 ML thin film of Fe that exhibits an in-plane direction of magnetization is used. This film is deposited at room temperature and upon completion heated up to approximately 550 K for 4 minutes. It is reported in literature that this last heating step stabilizes the magnetic layer and increases the change of successfully generating a magnetic tip [16, 74, 76].

## Chapter 8

# Collection of STM-induced luminescence

Another way to extract information about the local magnetization of the surface beneath an STM-tip is, as explained in section (2.4), through the collection and analysis of the STM-induced luminescence. Ideally, the STM-induced luminescence would be collected by a fiber that is installed in close proximity to the sample surface [77]. However, due to geometrical constraints this STM-induced luminescence collection scheme is not possible in the Omicron low temperature STM. The geometrical constraints imposed by the STM are depicted in figure 8.1. As can be seen the distance of closest approach to the center of the sample surface is 8.6 mm. If at this distance a single fiber collection system would be used, the intensity of the collected STM-induced luminescence would be far too low to be of any use.

### 8.1 Lens selection

To circumvent the problems associated with the large sample–fiber distance imposed by the Omicron low temperature STM, a lens / fiber luminescence collection system has been designed. With a lens / fiber collection scheme it should be possible to achieve a level of STM-induced luminescence collection that can rival that of a single fiber installed close to the sample surface. Obviously, a lens / fiber combination requires a lens with the right focal point to make this luminescence collection scheme work; high collection needs have to be traded off with indifference to poor alignment of the sample with respect to the lens. Furthermore, the dimensions of the lens are restricted by the available space in the Omicron low temperature STM. A first selection of commercially available lenses that more or less have the right focal lengths and suitable dimensions, see table 8.1, was made by use of the lens maker's formula. However, due to the combination of the small dimensions, required focal length, and the as-

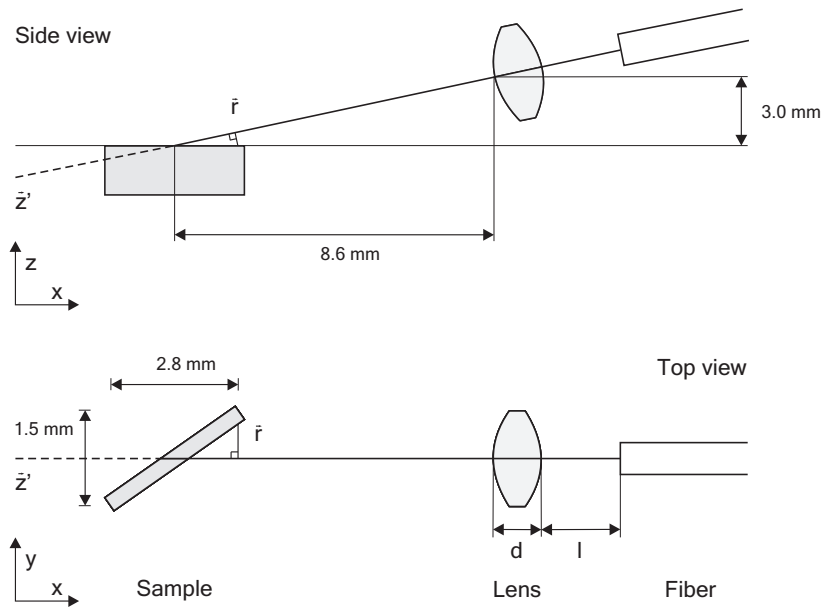


**Figure 8.1:** Geometry of the sample / lens / fiber system. The distance of the lens to the sample and the angle of  $\vec{z}'$  with respect to the sample are restricted by the geometry of the Omicron low temperature STM. The vector  $\vec{r}$  is perpendicular to the vector  $\vec{z}'$  which coincides with the middle of both lens and fiber. The distance between lens and fiber is given by  $l$ .

spheric surfaces of the evaluated lenses, it proved not possible to determine which lens is most suitable by means of the lens maker's formula. Therefore, a C++ program that can trace rays of light through the lens / fiber combination was written (see appendix A for the source code). In this program the numerical aperture, refractive index, and the shape of the lens surfaces have to be specified. Subsequently, these parameters are used by the program to trace rays of light emanating from an ideal point light source at a specified position through the lens / fiber combination. In figure 8.2, the output of the ray trace program in the so-called single point visualization mode is depicted for one of the evaluated lens / fiber combinations. By tracing a high number of light rays, typically a few thousand, and subsequently counting the number of light rays that incident onto the fiber and satisfy its numerical aperture, the magnitude of the solid angle of light collection  $\Omega$  can precisely be determined.

In order to evaluate the region in which a reasonable level of STM-induced luminescence collection can be achieved, the ray trace program is run in the so-called field mode in which the solid angle of collection is determined for a grid of points spanning an area in front of the lens / fiber combination. In figure 8.2 and figure 8.3 (top), respectively a typical output of the single point visualization mode and the field mode is shown. By varying the lens–fiber distance,

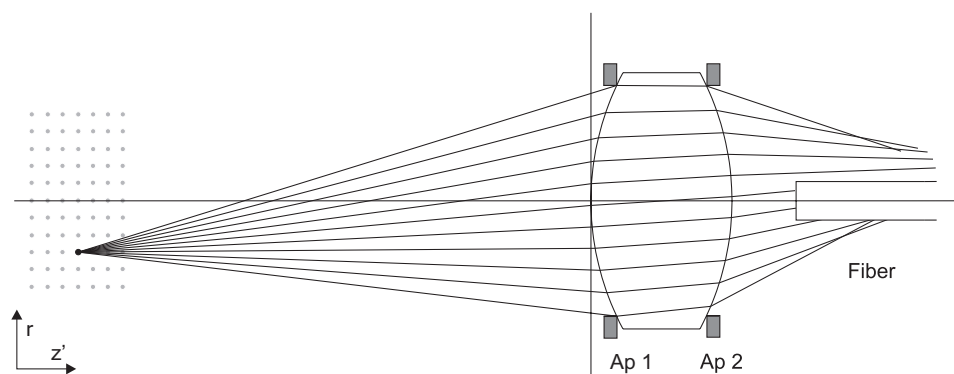


**Figure 8.2:** Output of the ray trace program in single point visualization mode. For reasons of clarity only eleven rays are traced through the lens. The number of rays that incident onto the fiber and satisfy the numerical aperture of the fiber are counted by the program. In field mode, the ray trace program determines the solid angle of light collection by the fiber as a function of the  $z'$  and  $r$  position in an area in front of the lens.

$l$ , the optimal lens / fiber configuration for every selected lens is determined. Subsequently, the length of the sample,  $s$ , that significantly contributes to the collected STM-induced luminescence is determined for this optimal lens-fiber distance. The results are presented in table 8.1. The best commercially available lens / fiber combination proofed to be the Geltech<sup>TM</sup> 350350 lens placed at a distance of 6 mm in front of the fiber. This lens has the highest solid angle of light collection of all evaluated lenses and still has a reasonable sample length over which the STM-induced luminescence can be collected.

In figure 8.3 (top), the by the ray trace program determined solid angle of light collection  $\Omega$  as a function of the position of an ideal point light source in front of the Geltech<sup>TM</sup> 350350 lens / fiber collection system is depicted. The black bar represents the top of the cleaved sample. As can be seen, the part of the sample that can significantly contribute to the captured STM-induced luminescence is bounded by steep gradients in  $\Omega$  and evaluates to  $s = 1.00$  mm. The solid angle of light collection is found to be in the range of  $\Omega = 6.9\text{--}10.4 \times 10^{-2}$  sr on this part of the sample.

## 8.2 Experimental validation

In order to experimentally check whether the selected lens / fiber combination satisfies the simulations of the ray trace program, the intensity of the collected light as a function of the position of a point light source in front of the selected lens / fiber combination was measured. A  $40 \mu\text{m}$  pinhole, that could be moved by a xyz-stage, was used to resemble the ideal point light source as assumed by the ray trace program. In figure 8.3 (bottom), the experimentally measured

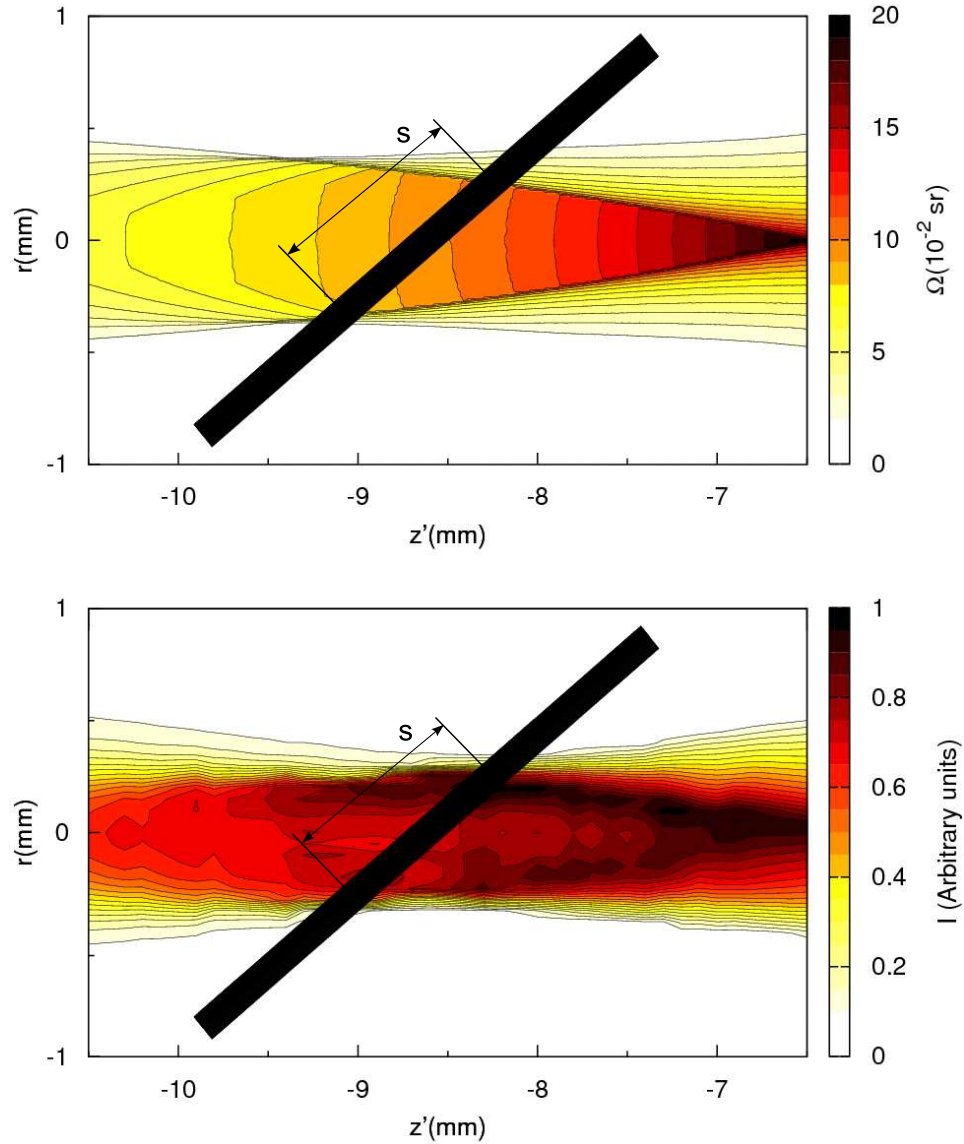


**Figure 8.3:** Simulated solid angle of light collection (top) and measured intensity of the collected light (bottom) as a function of the position of a point light source in front of the Geltech<sup>TM</sup> 350350 lens / fiber combination. The black bar represents the top of the cleaved sample. The length of the sample,  $s$ , that can significantly contribute to the captured STM-induced luminescence is bounded by step gradients in respectively  $\Omega$  and  $I$ . As can be seen, the pattern of the intensity of the collected light closely matches that of the simulated solid angle of light collection.

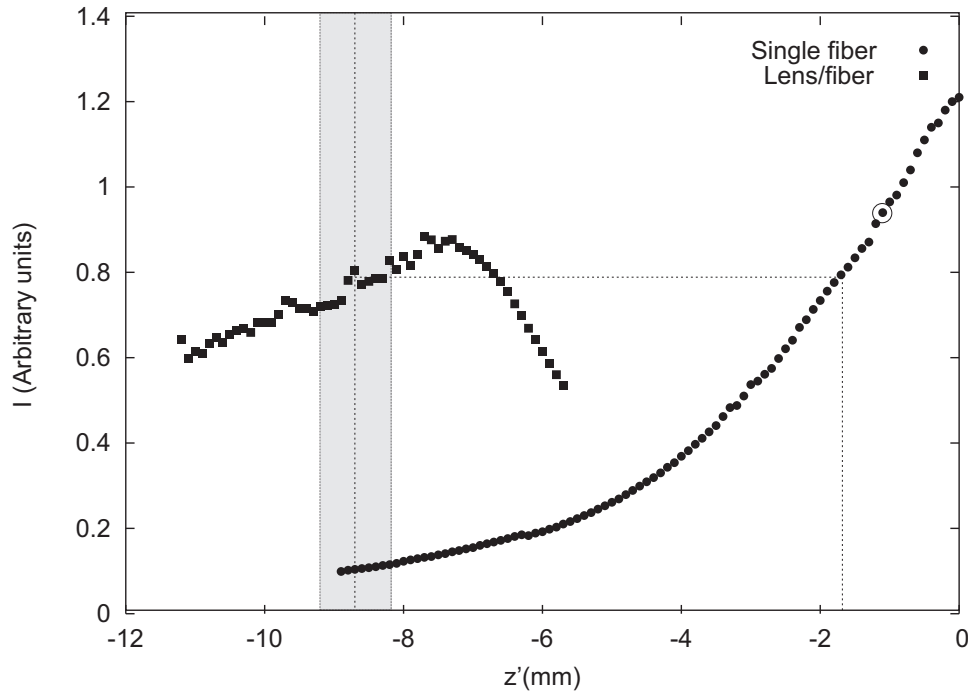


**Figure 8.4:** Comparison of the intensity of the collected light  $I$  as a function of the point light source's position on the optical axis as measured for a single fiber and the selected lens/fiber combination. The gray area represent the length of the sample that can significantly contribute to the collected STM-induced luminescence. With the lens / fiber combination a level of luminescence collection equal to that of a single fiber placed approximately 1.7 mm from the sample surface can be reached (see dashed lines). The collection efficiency of a successfully used single fiber STM-induced luminescence collection system [77] is denoted by the circle.

intensity of the collected light,  $I$ , as a function of the position of the point light source in front of the lens / fiber combination is depicted. As can be seen, the measured pattern of the intensity of the collected light closely resembles the pattern of the solid angle of light collection as obtained by use of the ray trace program. Any discrepancies between the two patterns are most likely due to the lens clamping mechanism used, which is not completely symmetrical and reflects some of the light emanating from the point light source, and slight misalignments in the experimental setup.












In order to determine whether the selected lens / fiber combination can rival a single fiber as an STM-induced luminescence collection system, the intensity of the collected light as a function of the point light source's position on the optical axis was measured for both systems. Figure 8.4 shows the intensity as a function of the point light source's position on the optical axis,  $I(z')$ , for both the lens / fiber collection system and the single fiber collection system. The gray area represents the part of the sample,  $s$ , that can significantly contribute to



the collected STM-induced luminescence. As can be seen, the highest level of STM-induced luminescence collection that can be obtained with the lens / fiber combination is reached at a position of approximately 8.2 mm in front of the collection system. At this distance, the lens / fiber collection system yields a 8 fold increase in collection efficiency as compared to a single fiber collection system. If the highest reached level of light collection is compared with the level of light collection of the single fiber, it turns out that the lens / fiber STM-induced luminescence collection system is equivalent to a single fiber that is placed at a distance of approximately 1.7 mm from the light source. In order to get an indication whether the lens / fiber collection system will work, it is compared to a single fiber STM-induced luminescence collection system that has been successfully used [77]. In this collection system the distance between the fiber and the sample is 1.1 mm. If at this distance, the collection efficiency that was measured for the single fiber is compared to the collection efficiency of the selected lens / fiber collection system, see figure 8.4, a reduction in collection efficiency of approximately 15% is found. Such a small reduction in collection efficiency is a good reason to believe that the designed lens / fiber collection system will indeed work in the Omicron low temperature STM.

From figure 8.4 it can be seen that a trade off between light collection and indifference to misalignment has been made; the interval in which the sample can significantly contribute to the collected light is not the interval in which the highest light collection can be achieved. However, in this interval a large part of the sample,  $s = 1$  mm, is available on which the STM-induced luminescence can be detected. The observed decrease in intensity of the collected light of the lens / fiber combination at distances smaller than approximately 7 mm is due to the limited numerical aperture of both the lens and the fiber.

**Table 8.1:** Diameter  $\phi$ , thickness  $d$ , and focal length  $f$  of all the evaluated lenses as specified by the manufacture. The optimal distance of the fiber behind the lens,  $l$ , is determined by the use of a ray trace program. For the optimal distance the length of sample that can significantly contribute to the captured STM-induced luminescence,  $s$ , is determined. The range of solid angle which can be captured on this part of the sample is given by  $\Omega$ .

	Linus G312004000, Plano-convex $\phi = 3.00$ mm $d = 1.50$ mm	$l = 2.75$ mm $d + l = 4.25$ mm	$f = 3$ mm $\Omega = 1.5\text{--}2.9 \times 10^{-2}$ sr $s = 1.90$ mm
	Linus G312005000, Plano-convex $\phi = 3.50$ mm $d = 1.75$ mm	$l = 3.25$ mm $d + l = 5.00$ mm	$f = 3.5$ mm $\Omega = 2.9\text{--}4.2 \times 10^{-2}$ sr $s = 1.20$ mm
	Linus G312006000, Plano-convex $\phi = 4.00$ mm $d = 2.00$ mm	$l = 4.25$ mm $d + l = 6.25$ mm	$f = 4$ mm $\Omega = 4.0\text{--}5.7 \times 10^{-2}$ sr $s = 1.10$ mm
	Linus G312007000, Plano-convex $\phi = 5.00$ mm $d = 2.50$ mm	$l = 6.00$ mm $d + l = 8.50$ mm	$f = 5$ mm $\Omega = 7.7\text{--}9.1 \times 10^{-2}$ sr $s = 0.40$ mm
	Thorlabs 350140, Aspheric $\phi = 2.40$ mm $d = 1.01$ mm	$l = 2.00$ mm $d + l = 3.01$ mm	$f = 1.45$ mm $\Omega = 0.4\text{--}0.8 \times 10^{-2}$ sr $s = 3.00$ mm
	Thorlabs 350200, Aspheric $\phi = 2.40$ mm $d = 1.03$ mm	$l = 0.50$ mm $d + l = 1.53$ mm	$f = 1.14$ mm $\Omega = 0.2\text{--}0.4 \times 10^{-2}$ sr $s = 3.00$ mm
	Thorlabs 350350, Aspheric $\phi = 4.70$ mm $d = 3.66$ mm	$l = 6.00$ mm $d + l = 9.66$ mm	$f = 4.5$ mm $\Omega = 6.9\text{--}10.4 \times 10^{-2}$ sr $s = 1.00$ mm
	Thorlabs 350550, Aspheric $\phi = 2.40$ mm $d = 1.75$ mm	$l = 8.75$ mm $d + l = 10.50$ mm	$f = 6.1$ mm $\Omega = 1.9\text{--}2.7 \times 10^{-2}$ sr $s = 1.00$ mm
	Melles Griot LDX 401, Bi-convex $\phi = 5.00$ mm $d = 2.00$ mm	$l = 6.25$ mm $d + l = 8.25$ mm	$f = 4.5$ mm $\Omega = 6.1\text{--}9.1 \times 10^{-2}$ sr $s = 0.85$ mm
	Sigma Koki SLM-03B-03P, Bi-convex $\phi = 3.00$ mm $d = 1.80$ mm	$l = 3.25$ mm $d + l = 5.05$ mm	$f = 3$ mm $\Omega = 1.9\text{--}3.6 \times 10^{-2}$ sr $s = 1.80$ mm
	Sigma Koki SLM-04B-04P, Bi-convex $\phi = 4.00$ mm $d = 2.20$ mm	$l = 4.75$ mm $d + l = 6.95$ mm	$f = 4$ mm $\Omega = 4.0\text{--}6.3 \times 10^{-2}$ sr $s = 1.20$ mm



## Chapter 9

# Conclusion & outlook

The aim of this thesis was the demonstration of spin-polarized tunneling in the in house Omicron low temperature STM. To this end, it was decided to replicate a well documented experiment in which thin layers of ferromagnetic material are deposited on a tungsten W(110) surface. In case 1–2 monolayers of iron are deposited on a slightly miscut W(110) crystal, the surface will exhibit an alternating in-plane / out-of-plane direction of magnetization, resulting in high magnetic contrast on the nanometer scale. An advantage of such a surface is that, once spin-polarized tunneling microscopy (SP-STM) has been demonstrated, it will be an ideal surface for characterizing magnetic tips for future measurements.

The chosen approach to demonstrate spin-polarized tunneling requires several conditions to be fulfilled. First of all, the W(110) surface on which the thin magnetic film is to be deposited has to be clean. For this purpose, a high temperature oven capable of sustained heating of the W(110) surface to  $\approx 1700$  K and flashing up to  $\approx 2300$  K has successfully been designed, build, and tested. The high temperature oven fulfilled, and even exceeded, its design specifications; it proofed possible to deposited 400 W on the sample. As it turned out, this amount of power is more than enough for removing the oxide layer and all the adsorbates on the surface. The cleanliness of the surface has been checked by means of STM topography and  $I-V$  spectroscopy, which showed the same characteristic metallic behavior for the entire W(110) surface.

The second condition that has to be met, is the ability to deposit controlled quantities of ferromagnetic material on both the W(110) surface and the tips. For this purpose, two Omicron EFM3 evaporators were fitted with chromium and iron evaporation rods which were successfully calibrated by measuring step profiles of the deposited material with an AFM. It was demonstrated by STM measurements that post annealing the Fe / W(110) sample to  $\approx 550$  K for 4 minutes, step flow growth, which is required for the formation of the alternating in-plane / out-of-plane direction of magnetization, could be achieved.

The third and final requirement for successful demonstration of spin-polarized tunneling, is the ability to reproducibly generate magnetic tips. Instead of using

a sharp tip consisting of bulk (anti)-ferromagnetic material, the tips used in this project are tips that have a blunt apex,  $\approx 500$  nm, covered with 3–10 ML of iron. In this way the surface and interface anisotropy of the thin film, and thus the direction of magnetization of the tip, can be controlled. Several methods for the *in situ* preparation of these blunt tips have been tried but proved all to be unsuccessful. Therefore, an *ex situ* etching procedure has been developed that reproducibly yields tip with an apex diameter of  $\approx 500$  nm.

With all three conditions met, the demonstration of spin-polarized tunneling in the Omicron low temperature seemed within grasp. However, in the final stage of this project, or more precisely at the very moment that both the Fe/W(110) sample and the magnetic tips had successfully been prepared, the STM broke down. At the moment of printing the STM is still not operational again. Although a successful demonstration of SP-STM could have been the crowning glory on all the work done during this master thesis, much was learned in the course of this project and it will be a matter of time before SP-STM is achieved.

In addition to the approach of directly detecting spin by means of the tunneling current, another option to detect spin-polarized tunneling has been pursued during this project; collection and analysis of the STM-induced luminescence. Depending on the relative direction of magnetization of sample and tip, the by the STM tip induced photons will be left or right circular polarized. The approach commonly used to collect STM-induced luminescence is by means of installing a fiber in close proximity to the sample. Due to geometrical constraints this approach is not possible in the case of the Omicron low temperature STM. To solve this problem a lens / fiber collection has been designed. For the purpose of selecting the best commercially available lens, a ray trace program with which rays of light could be traced through the system has been written. After careful examination of dozens of lenses, the Thorlabs 350350 aspheric lens proved to be the best choice. The light collection characteristics as predicted by the ray trace program have been experimentally validated.

To conclude, a brief outlook to the future. As mentioned above, demonstration of spin-polarized tunneling in the Omicron low temperature STM is only a matter of time. The first, and to my opinion only, thing that has to be done is repairing the broken STM. With the STM back in operation, spin-polarized tunneling should be demonstrated within a week or two. However, one thing learned during this project is that any time frame for experimental work should at least be multiplied by a factor two to account for unforeseen problems. A more realistic time frame in which spin-polarized tunneling could be demonstrated would therefore be 1–2 months. Although the breakdown of the STM was, to say the least, very frustrating, it has one advantage: the lens / fiber combination that has been designed for the collection of the STM-induced luminescence can be installed during the repairs. Aligning of the optics would probably take one week, after which the system can be *in situ* tested. Within 1–2 months it should be possible to demonstrate the collection of STM-induced luminescence by the lens / fiber combination.

## Chapter 10

# Acknowledgments

First of all, I would like to thank my parents for their support during all the years of my study. It is hard to imagine how I could have finished this study without their support. Secondly, I would like to thank my girlfriend Haike van Stralen, who always showed great interest in my study, graduation thesis, and physics in general. At times, the questions she asked made me realize that most things in physics are not as simple as they may appear at first sight.

This work could not have been done without the support of numerous people in the Photonics Semiconductors and Nanophysics group. In particular, I would like to thank Peter Nouwens, Tom Eijkemans, and Jos van Ruijven who were of great help to me. Furthermore, I would like to thank all the people from the Photonics Semiconductors and Nanophysics group for making me feel at home right from the beginning of my graduation project. A special word of thanks to Margriet van Doorne for having a big part in this. Although not part of the Photonics Semiconductors and Nanophysics group, I would like to thank Gerard Wijers, for his extremely useful advice, facilitating his equipment, and supplying materials when ordering them would have taken a long time.

Last but certainly not least, I want to thank both my supervisors. First Paul Koenraad for giving me the opportunity to do my graduation project in this group. Furthermore, I would like to thank him for his enthusiasm and warm manner of communicating which made me feel right at home and appreciated. My special thanks go out to my direct supervisor Jens Garleff. I learned a great deal from him both experimentally and theoretically. It is very much appreciated that he almost always instantaneously could find the time to help me with the numerous problems I encountered during the past year. Many thanks for this.

To conclude, I would like to say that I feel very lucky and grateful to start my promotion in this group. I look forward to working in this group and hope that the next four years will be just as nice as the past year has been. Thank you all.



## Appendix A

# Ray trace program

**Listing A.1:** C++ source code of the ray trace program that was written to select the best commercially available lens for use in the lens / fiber STM-induced luminescence collection system. The program as listed below is configured for the Thorlabs 350350 aspheric lens.

```

1  /*****
2  /* C++ program to trace rays emitted by a point source through a lens into
3  /* a fiber. The program takes into account the numerical aperture on both
4  /* sides of the lens and the numerical aperture of the fiber. The surfaces
5  /* of the lens can be specified by functions. All the by the fiber collected
6  /* total angles as a function of position in front of the lens and fiber
7  /* distance behind the lens are written to data files. J.G.Keizer, 2007
8  *****/
9
10 #include <cstdlib>
11 #include <iostream>
12 #include <fstream>
13 #include "math.h"
14 #include "string.h"
15
16 /*****
17 /* Plot settings. If bool ray_trace=true the program traces a specified
18 /* number of rays through the lens and outputs the lens system and the ray
19 /* trace data to "ray_trace.dat". This setting can be used for debugging.
20 /* If bool ray_trace=false the program calculates the total collected angles
21 /* as a function of position in front of the lens and fiber distance behind
22 /* the lens. The results are written to "results_<fiber distance>.dat".
23 *****/
24
25 using namespace std;
26
27 // ray trace mode settings
28 const bool ray_trace=false; // ray trace mode switch
29 const bool plot_normals=false; // option to draw normals
30 const double ray_trace_fib_pos=255; // fiber position in ray trace mode
31 const double ray_trace_x_pos=-14.8; // object position in ray trace mode
32 const double ray_trace_y_pos=0;
33
34 // numerical settings
35 const double step_size= 0.05; // step size in evaluated field
36 const double total_rays= 301; // numbers of ray in fan
37 const double tol= 0.001; // solving precision
38 const double x_field_1 = -10.5; // dimensions of the evaluated field in
39 const double x_field_2 = -7; // front of the lens
40 const double y_field_1 = -1;
41 const double y_field_2 = 1;
42 const double min_fib_pos = 1.00; // mininum fiber-lens distance
43 const double max_fib_pos = 9.00; // maximum fiber-lens distance
44 const double fib_step_size = 0.25; // step size of fiber position
45
46 // fiber constants
47 const double fib_wid = 0.6; // fiber width
48 const double fib_ap = 12.709; // numerical aperture of fiber in degree
49

```



```

50 // global constants
51 const bool inverted = true;           // invert lens switch
52 const double n_gas = 1.0;           // refractive index of the gas
53 const double Pi = 3.14159265;
54
55 // Clens class that can hold all lens information
56 class Clens
57 {
58 public:
59     string name;
60     double n;
61     double tc;
62     double d;
63     class Csurface
64     {
65     public:
66         double R;
67         double a4;
68         double a6;
69         double a8;
70         double a10;
71         double k;
72         double ap;
73     };
74     Csurface s1;
75     Csurface s2;
76 };
77
78 // list of variables that hold the lens data
79 Clens l_350350;           // Thorlabs 350350
80 Clens act_lens;         // The active lens has to be specified in the second line
81                        // of the main program.
82
83 /*****
84 /*
85 /*  FUNCTIONS
86 /*
87 /*****
88
89 // initialize lens definitions
90 void init_lens_data ()
91 {
92     l_350350.name = "Thorlabs_350350";
93     l_350350.n = 1.597;
94     l_350350.tc = 3.655;
95     l_350350.d = 4.70;
96     l_350350.s1.R = 2.8797745;
97     l_350350.s1.a4 = 3.14802762e-4;
98     l_350350.s1.a6 = -2.54647053e-5;
99     l_350350.s1.a8 = -2.81435764e-6;
100    l_350350.s1.a10 = -3.30733580e-7;
101    l_350350.s1.k = -0.6415948;
102    l_350350.s1.ap = 4.7;
103    l_350350.s2.R = 19.136;
104    l_350350.s2.a4 = 0;
105    l_350350.s2.a6 = 0;
106    l_350350.s2.a8 = 0;
107    l_350350.s2.a10 = 0;
108    l_350350.s2.k = 0;
109    l_350350.s2.ap = 4.7;
110 }
111
112 // Return the x-position of a point on a line given by a starting point,
113 // vector, and y-position
114 double line(double m_in[2], double vec[2], double y)
115 {
116     return vec[0]/vec[1]*(y-m_in[1])+m_in[0];
117 }
118
119 // Plot a line from points m_in to m_out
120 void plot_line(double m_in[2], double m_out[2], ofstream &dout)
121 {
122     dout << m_in[0] << "\t" << m_in[1] << endl;
123     dout << m_out[0] << "\t" << m_out[1] << endl << endl;
124 }
125
126 // Calculate the angle between two vectors
127 double angle(double vec_1[2], double vec_2[2])
128 {
129     return acos((vec_1[0]*vec_2[0]+vec_1[1]*vec_2[1])/(sqrt(vec_1[0]*vec_1[0]
130     +vec_1[1]*vec_1[1])*sqrt(vec_2[0]*vec_2[0]+vec_2[1]*vec_2[1])));
131 }
132
133 // Snell's law

```

```

134 double snell(double ang, double n_in, double n_out)
135 {
136     return asin(n_in/n_out*sin(ang));
137 }
138
139 // Return the x-value of a y-value on the specified lens surface
140 double lens(double y, string surface)
141 {
142     double x;
143     double R, k, a4, a6, a8, a10;
144     if (surface=="1")
145     {
146         R=act_lens.s1.R;
147         k=act_lens.s1.k;
148         a4=act_lens.s1.a4;
149         a6=act_lens.s1.a6;
150         a8=act_lens.s1.a8;
151         a10=act_lens.s1.a10;
152     }
153     else
154     {
155         R=act_lens.s2.R;
156         k=act_lens.s2.k;
157         a4=act_lens.s2.a4;
158         a6=act_lens.s2.a6;
159         a8=act_lens.s2.a8;
160         a10=act_lens.s2.a10;
161     }
162     x=act_lens.tc-(y*y/(R*(1+sqrt(1-((1+k)*y*y)/(pow(R,2))))))+a4*pow(y,4)
163     +a6*pow(y,6)+a8*pow(y,8)+a10*pow(y,10));
164     // take into account that the lens can be inverted
165     if ((surface=="1") and (inverted==false)){x=act_lens.tc-x;}
166     if ((surface=="2") and (inverted==true)){x=act_lens.tc-x;}
167     return x;
168 }
169
170 // calculate the normal [1,y] on the specified lens surface.
171 double calc_normal(double y, string surface)
172 {
173     double x;
174     double R, k, a4, a6, a8, a10;
175     if (surface=="1")
176     {
177         R=act_lens.s1.R;
178         k=act_lens.s1.k;
179         a4=act_lens.s1.a4;
180         a6=act_lens.s1.a6;
181         a8=act_lens.s1.a8;
182         a10=act_lens.s1.a10;
183     }
184     else
185     {
186         R=act_lens.s2.R;
187         k=act_lens.s2.k;
188         a4=act_lens.s2.a4;
189         a6=act_lens.s2.a6;
190         a8=act_lens.s2.a8;
191         a10=act_lens.s2.a10;
192     }
193     x=2*y/(R*(1+sqrt(1-((1+k)*y*y)/(pow(R,2)))))+pow(y,3)*(1+k)/( pow(R,3)
194     *(1+sqrt(1-((1+k)*y*y)/(pow(R,2))))*(1+sqrt(1-((1+k)*y*y)/(pow(R,2))))))
195     -4*a4*pow(y,3)-6*a6*pow(y,5)-8*a8*pow(y,7)-10*a10*pow(y,9);
196     // take into account that the lens can be inverted
197     if (inverted){x=-x;}
198     return x;
199 }
200
201 // Return f(y)=line(y)-lens(y) as used in the numerical solving scheme
202 double f(double m.in[2], double vec[2], double y, string surface)
203 {
204     return line(m.in, vec,y)-lens(y, surface);
205 }
206
207 // Numerically evaluate where a ray, given by a starting point and vector,
208 // intersects a specified lens surface. A variation of Newton's method is used
209 // as the numerical scheme.
210 double solve(double m.in[2], double vec.in[2], string surface, double angle.in)
211 {
212     double y1,y2,y3;
213     y1=act_lens.d/2-1;
214     y2=act_lens.d/2-0.5;
215     y3=act_lens.d;
216     while (fabs(y3-y2)>tol)
217     {

```

```

218     y1=y2;
219     y2=y3;
220     y3=y2-f(m.in, vec.in, y2, surface)*(y2-y1)/(f(m.in, vec.in, y2, surface)
221         -f(m.in, vec.in, y1, surface));
222 }
223 return y3;
224 }
225
226 // Plot the lens system to "ray_trace.dat"
227 void plot_system(ofstream &dout)
228 {
229     // x-axis
230     dout<<"-50_\t_0"<<endl;
231     dout<<"350_\t_0"<<endl<<endl;
232     // y-axis
233     dout<<"0_\t_-40"<<endl;
234     dout<<"0_\t_40" <<endl<<endl;
235     // first (left) lens
236     for (double y=-act_lens.d/2;y<=act_lens.d/2+tol;y+=0.1)
237     {
238         dout<<lens(y,"1")<<"\t"<<y<< endl;
239     }
240     dout << endl;
241     // second (right) lens
242     for (double y=-act_lens.d/2;y<=act_lens.d/2+0.1;y+=0.1)
243     {
244         dout<<lens(y,"2")<<"\t"<<y<<endl;
245     }
246     dout<<endl;
247     // top part of lenses
248     dout<<lens(act_lens.d/2,"1")<<"\t"<<act_lens.d/2<<endl;
249     dout<<lens(act_lens.d/2,"2")<<"\t"<<act_lens.d/2<<endl<<endl;
250     dout<<lens(act_lens.d/2,"1")<<"\t"<<-act_lens.d/2<<endl;
251     dout<<lens(act_lens.d/2,"2")<<"\t"<<-act_lens.d/2<<endl<<endl;
252     // fiber
253     dout<<ray_trace_fib_pos+2+act_lens.tc<<"\t"<<fib_wid/2<<endl;
254     dout<<ray_trace_fib_pos+act_lens.tc<<"\t"<<fib_wid/2<<endl;
255     dout<<ray_trace_fib_pos+act_lens.tc<<"\t"<<-fib_wid/2<<endl;
256     dout<<ray_trace_fib_pos+2+act_lens.tc<<"\t"<<-fib_wid/2<<endl<<endl;
257     // lens apertures
258     dout<<lens(act_lens.s1.ap/2,"1")<<"\t"<<act_lens.d/2<<endl;
259     dout<<lens(act_lens.s1.ap/2,"1")<<"\t"<<act_lens.s1.ap/2<<endl<<endl;
260     dout<<lens(-act_lens.s1.ap/2,"1")<<"\t"<<-act_lens.d/2<<endl;
261     dout<<lens(-act_lens.s1.ap/2,"1")<<"\t"<<-act_lens.s1.ap/2<<endl<<endl;
262     dout<<lens(act_lens.s2.ap/2,"2")<<"\t"<<act_lens.d/2<<endl;
263     dout<<lens(act_lens.s2.ap/2,"2")<<"\t"<<act_lens.s2.ap/2<<endl<<endl;
264     dout<<lens(-act_lens.s2.ap/2,"2")<<"\t"<<-act_lens.d/2<<endl;
265     dout<<lens(-act_lens.s2.ap/2,"2")<<"\t"<<-act_lens.s2.ap/2<<endl<<endl;
266 }
267
268 /*****
269 /*
270 /* MAIN PROGRAM
271 /*
272 /*****
273
274 int main()
275 {
276     init_lens_data(); // initialize the lens data
277     act_lens=l.350350; // select active lens
278     string surface_1, surface_2;
279     double m_in_1[2], normal[2], m_in[2], m_out[2], vec[2], vec_2[2], vec_1[2];
280     double final_ang, ang_in_n, ang_out_n, ang_in_axis, ang_n_axis, ang_out_axis;
281     double y_fib_plane, step_counter, collected, angle_in, angle_in_bot, angle_in_top;
282     double m_fib_start, m_fib_end, fib_pos, ap1, ap2, x_start, x_end, y_start, y_end;
283     double total_steps=((x_field_2-x_field_1)/step_size+1)
284         *((y_field_2-y_field_1)/step_size+1);
285     // if ray trace mode selected, only one fiber position is evaluated
286     if (ray_trace)
287     {
288         m_fib_start=ray_trace_fib_pos;
289         m_fib_end=ray_trace_fib_pos;
290     }
291     else
292     {
293         m_fib_start=min_fib_pos;
294         m_fib_end=max_fib_pos;
295     }
296     // evaluate for selected fiber positions
297     for (double m=m_fib_start;m<=m_fib_end;m+=fib_step_size)
298     {
299         //file handling
300         ofstream dout, result;
301         char str1[10], str2[10], zero[2], buf_str[3];

```

```

302 strcpy (zero, "00");
303 strcpy (str1, "result_");
304 strcpy (str2, ".dat");
305 int buf_int=round(m*100);
306 itoa(buf_int, buf_str, 10);
307 if ((buf_int < 100) and (buf_int != 0))
308 {
309     if (buf_int < 10)
310     {
311         strncat (str1, zero, 2);
312         strncat (str1, buf_str, 1);
313     }
314     else
315     {
316         strncat (str1, zero, 1);
317         strncat (str1, buf_str, 2);
318     }
319 }
320 if (buf_int == 0)
321 {
322     strncat (str1, "000" , 3);
323 }
324 if (buf_int >= 100)
325 {
326     strncat (str1, buf_str, 3);
327 }
328 strncat (str1, str2, 4);
329 result.open(str1, ios::trunc);
330 // a step counter is used to track the progress
331 step_counter=0;
332 if (ray_trace)
333 {
334     dout.open ("ray_trace.dat", ios::trunc);
335     plot_system(dout);
336     fib_pos=ray_trace.fib_pos+act.lens.tc;
337     x_start=ray_trace.x_pos;
338     y_start=ray_trace.y_pos;
339     x_end=ray_trace.x_pos;
340     y_end=ray_trace.y_pos;
341 }
342 else
343 {
344     fib_pos=m+act.lens.tc;
345     x_start=x.field_1;
346     y_start=y.field_1;
347     x_end=x.field_2;
348     y_end=y.field_2;
349 }
350 // if the lens is inverted, invert the surfaces and apertures
351 if (inverted)
352 {
353     surface_1="2";
354     surface_2="1";
355     ap1=act.lens.s2.ap;
356     ap2=act.lens.s1.ap;
357 }
358 else
359 {
360     surface_1="1";
361     surface_2="2";
362     ap1=act.lens.s1.ap;
363     ap2=act.lens.s2.ap;
364 }
365 // evaluate for the selected field
366 for (double x=x_start; x<=x_end; x+=step_size)
367 {
368     for (double y=y_start; y<=y_end; y+=step_size)
369     {
370         step_counter++;
371         // verbose progress
372         cout << str1 << "_Done_:_" << round(step_counter/total_steps*100)
373             << "%\r" ;
374         // determine vectors from object point to bottom and top of
375         // lens aperture
376         m.in[0]=x;
377         m.in[1]=y;
378         m.out[1]=ap1/2;
379         m.out[0]=lens(m.out[1], surface_1);
380         vec_1[0]=m.out[0]-m.in[0];
381         vec_1[1]=m.out[1]-m.in[1];
382         m.out[1]=-ap1/2;
383         m.out[0]=lens(m.out[1], surface_1);
384         vec_2[0]=m.out[0]-m.in[0];
385         vec_2[1]=m.out[1]-m.in[1];

```

```

386     angle_in=angle(vec_1,vec_2);
387     angle_in_top=atan(vec_1[1]/vec_1[0]);
388     angle_in_bot=atan(vec_2[1]/vec_2[0]);
389     collected=0;
390     // evaluate for selected number of angles
391     for (double ang=angle_in_bot; ang<=angle_in_top+tol; ang+=angle_in
392         /(total_rays-1))
393     {
394         // rays from object point to first lens surface
395         vec[0]=cos(ang);
396         vec[1]=sin(ang);
397         m_out[1]=solve(m_in,vec,surface_1,angle_in);
398         m_out[0]=lens(m_out[1],surface_1);
399         if (ray_trace)
400         {
401             plot_line(m_in, m_out, dout);
402         }
403         // calculate and draw normals of first surface
404         normal[0]=-1;
405         normal[1]=calc_normal(m_out[1],surface_1);
406         // take into account that the lens can be inverted
407         if (inverted==true) normal[1]=-normal[1];
408         if (plot_normals)
409         {
410             dout<<m_out[0]<<"\t"<<m_out[1]<<endl;
411             dout<<m_out[0]-1<<"\t"<<m_out[1]+normal[1]<<endl<<endl;
412         }
413         // calculate angle between normals and incident rays
414         vec[0]=-vec[0];
415         vec[1]=-vec[1];
416         ang_in_n=angle(normal,vec);
417         // calculate angle between normal and outgoing rays
418         ang_out_n=snell(ang_in_n, n_gas, act_lens.n);
419         // calculate angle between x-axis and incident rays
420         ang_in_axis=atan((m_out[1]-m_in[1])/(m_out[0]-m_in[0]));
421         // calculate angle between x-axis and normals
422         ang_n_axis=atan(normal[1]/normal[0]);
423         // calculate angle between x-axis and outgoing rays.
424         // note the difference between ang_n_axis<ang_in_axis and
425         // ang_n_axis>ang_in_axis.
426         if (ang_n_axis<ang_in_axis)
427         {
428             ang_out_axis=ang_out_n+ang_n_axis;
429         }
430         else
431         {
432             ang_out_axis=-ang_out_n+ang_n_axis;
433         }
434         ang_in_axis=ang_out_axis;
435         // rays from first surface to second surface
436         m_in_1[0]=m_out[0];
437         m_in_1[1]=m_out[1];
438         vec[0]=cos(ang_in_axis);
439         vec[1]=sin(ang_in_axis);
440         m_out[1]=solve(m_in_1,vec,surface_2,angle_in);
441         m_out[0]=lens(m_out[1],surface_2);
442         if (ray_trace)
443         {
444             plot_line(m_in_1, m_out, dout);
445         }
446         // calculate and draw normals of second surface
447         normal[0]=-1;
448         normal[1]=calc_normal(m_out[1],surface_2);
449         // take into account that the lens can be inverted
450         if (inverted==false) normal[1]=-normal[1];
451         if (plot_normals)
452         {
453             dout<<m_out[0]<<"\t"<<m_out[1]<<endl;
454             dout<<m_out[0]-1<<"\t"<<m_out[1]+normal[1]<<endl<<endl;
455         }
456         // calculate angle between normals and incident rays
457         vec[0]=-vec[0];
458         vec[1]=-vec[1];
459         ang_in_n=angle(normal,vec);
460         // calculate angle between normals and outgoing rays
461         ang_out_n=snell(ang_in_n, act_lens.n, n_gas);
462         // calculate angle between x-axis and incident rays
463         ang_in_axis=atan((m_out[1]-m_in_1[1])/(m_out[0]-m_in_1[0]));
464         // calculate angle between x-axis and normals
465         ang_n_axis=atan(normal[1]/normal[0]);
466         // calculate angle between x-axis and outgoing rays.
467         // note the difference between ang_n_axis<ang_in_axis and
468         // ang_n_axis>ang_in_axis.
469         if (ang_n_axis<ang_in_axis)

```

```

470     {
471         ang_out_axis=ang_out_n+ang_n_axis;
472     }
473     else
474     {
475         ang_out_axis=-ang_out_n+ang_n_axis;
476     }
477     // draw outgoing rays and check second aperature
478     if ( fabs(m.out[1]) > ap2/2)
479     {
480         if ( ray_trace)
481         {
482             dout<<m.out[0]<<"\t"<< m.out[1]<<endl;
483             dout<<lens(ap2/2,surface_2)<<"\t"<<m.out[1]-(m.out[0]
484             -lens(ap2/2,surface_2))*tan(ang_out_axis)<<endl<<endl;
485         }
486     }
487     else
488     {
489         // determine the y-position in the y-plane of the fiber
490         y_fib_plane=m.out[1]+(fib_pos-m.out[0])*tan(ang_out_axis);
491         if ((y_fib_plane>fib_wid/2) or (y_fib_plane<-fib_wid/2))
492         {
493             // ray does not end on fiber surface
494             if ( ray_trace)
495             {
496                 dout<<m.out[0]<<"\t"<<m.out[1]<<endl;
497                 dout<<m.out[0]+fib_pos*cos(ang_out_axis)<<"\t"
498                 <<m.out[1]+fib_pos*sin(ang_out_axis)<<endl<<endl;
499             }
500         }
501         else
502         {
503             // ray ends on fiber surface
504             if ( ray_trace)
505             {
506                 dout << m.out[0] << "\t" << m.out[1] << endl;
507                 dout << fib_pos << "\t" << m.out[1]
508                 +(fib_pos-m.out[0])*tan(ang_out_axis)
509                 << endl << endl;
510             }
511             // check fiber aperature
512             if ( fabs(ang_out_axis/Pi*180)<fib_ap)
513             {
514                 collected++;
515             }
516         }
517     }
518 }
519 if ( collected <=1)
520 {
521     final_ang=0;
522 }
523 else
524 {
525     // calculate the total collected angle by the fiber and
526     // convert to a solid angle
527     final_ang=2*Pi*cos(1-angle_in/(total_rays-1))*(collected-1)/2;
528 }
529 result << m.in[0] << "\t" << m.in[1] << "\t" << final_ang << endl;
530 }
531 result << endl;
532 }
533 if ( ray_trace){dout.close();}
534 result.close();
535 }
536 return EXIT_SUCCESS;
537 }

```



---

## Bibliography

- [1] G. Binnig and H. Rohrer. Scanning tunneling microscopy. *Helv. Phys. Acta*, 55:726, 1982.
- [2] G. Binnig, H. Rohrer, C. Gerber, and E. Weibel. Surface studies by scanning tunneling microscopy. *Phys. Rev. Lett.*, 49:57, 1982.
- [3] G. Binnig, H. Rohrer, C. Gerber, and E. Weibel.  $7\times 7$  reconstruction on Si(111) resolved in real space. *Phys. Rev. Lett.*, 50:120, 1983.
- [4] G. Binnig and H. Rohrer. Scanning tunneling microscopy from birth to adolescence. *Rev. Mod. Phys.*, 59:615, 1987.
- [5] E.K. Schweitzer D.M. Eigler. Positioning single atoms with a scanning electron microscope. *Nature*, 344:524, 1990.
- [6] I-W. Lyo and Ph. Avouris. Field-induced nanometer- to atomic-scale manipulation of silicon surfaces with the stm. *Science*, 253(5016):173, 1991.
- [7] Th. Schimmel, H. Fuchs, S. Akari, and K. Dransfeld. Nanometer-size surface modifications with preserved atomic order generated by voltage pulsing. *Appl. Phys. Lett.*, 58(10):1039, 1991.
- [8] R. Feynmann. "there's plenty of room at the botoom" (1959) this talk given at the annual meeting of the American Physical Society at the California Institute of Technology was first published in the February 1960 issue of Caltech's *engineering and science*, which owns the copyright. it has been made available on the web at <http://www.zyvex.com/nanotech/feynman.html> with their permission.
- [9] P. Bedrossian, D.M. Chen, K. Mortensen, and J.A. Golovchenko. Demonstration of the tunnel-diode effect on an atomic scale. *Nature*, 342:258, 1989.
- [10] I-W Lyo and Ph. Avouris. Negative differential resistance on the atomic scale: Implications for atomic scale devices. *Science*, 245(4924):1369, 1989.



- [11] D.T. Pierce. Spin-polarized electron microscopy. *Physica Scripta*, 38:291, 1988.
- [12] C. Schoenenberger and S.F. Alvarado. Observation of single charge carriers by force microscopy. *Phys. Rev. Lett.*, 65:3162, 1990.
- [13] D. Rugar, H.J. Mamin, P. Guethner, S.E. Lambert, J.E. Stern, I. McFadyen, and T. Yogi. Magnetic force microscopy: General principles and application to longitudinal recording media. *J. Appl. Phys.*, 68(3):1169, 1990.
- [14] S. Heinze, M. Bode, A. Kubetzka, O. Pietzsch, X. Nie, S. Blugel, and R. Wiesendanger. Real-space imaging of two-dimensional antiferromagnetism on the atomic scale. *Science*, 288:1805, 2000.
- [15] R. Wiesendanger, I.V. Shvets, D. Burgler, G. Tarrach, H-J. Guntherodt, J.M.D. Coey, and S. Graser. Topographic and magnetic-sensitive scanning tunneling microscope study of magnetite. *Science*, 255:583, 1992.
- [16] A. Kubetzka, M. Bode, O. Pietzsch, and R. Wiesendanger. Spin-polarized scanning tunneling microscopy with antiferromagnetic probe tips. *Phys. Rev. Lett.*, 88(5), 2002.
- [17] J. Tersoff and D.R. Hamann. Theory of the scanning tunneling microscope. *Phys. Rev. B*, 31(2):805, 1985.
- [18] J. Bardeen. Tunneling from a many-body point of view. *Phys. Rev. Lett.*, 6:57, 1960.
- [19] D.J. Griffiths. *Introduction to Quantum Mechanics*. Prentice Hall, New Jersey, 1995.
- [20] L.D. Landau and L.M. Lifshitz. *Quantum Mechanics*. Pergamon Press, Oxford, 1977.
- [21] A. Baratoff. Theory of scanning tunneling microscopy - methods and approximations. *Physica B.*, 127:143, 1984.
- [22] C.J. Chen. Effects of  $m \neq 0$  tip states in scanning tunneling microscopy: the explanations of corrugation reversal. *Phys. Rev. Lett.*, 69:1656, 1992.
- [23] C.F. Quate. Vacuum tunneling: A new technique for microscopy. *Physics today*, august:26, 1986.
- [24] C.J. Chen. Origin of atomic resolution on metal surfaces in scanning tunneling microscopy. *Phys. Rev. Lett.*, 65(4):448, 1990.
- [25] G. Binnig and H. Rohrer. Scanning tunneling microscopy. *IBM J. Res. Develop.*, 44(1):279, 2000.

- [26] S. Goudsmit and G.E. Uhlenbeck. Ersetzung der Hypothese vom unmechanischen Zwang durch eine Forderung bezüglich des inneren Verhaltens jedes einzelnen Elektrons / Replacement of the hypothesis of nonmechanical connection by an internal degree of freedom of the electron. *Naturw*, 13:953, 1925.
- [27] M. Johnson and J. Clarke. Spin-polarized scanning tunneling microscopy: Concept, design, and preliminary results from a prototype operated in air. *J. Appl. Phys.*, 67(10):6141, 1989.
- [28] R. Meservey and P.M. Tedrow. Spin-polarized electron tunneling. *Physics Reports*, 238(4):173, 1994.
- [29] M.W.J. Prins, R. Jansen, and H. van Kempen. Spin-polarized tunneling with gaas tips in scanning tunneling microscopy. *Phys. Rev. B.*, 53:8105, 1996.
- [30] E.C. Stoner. Collective electron ferromagnetism: li. energy and specific heat. *Roy. Soc. London A*, 169(938):339, 1939.
- [31] S. Heinze. First-principles theory of scanning tunneling microscopy applied to transition-metal surfaces. *Dissertation*, Hamburg (2000).
- [32] D. Wortmann, S. Heinze, P. Kurz, G. Bihlmayer, and S. Blugel. Resolving complex atomic-scale spin structures by spin-polarized scanning tunneling microscopy. *Phys. Rev. Lett.*, 86(18):4132, 1991.
- [33] P. Hohenberg and W. Kohn. Inhomogeneous electron gas. *Phys. Rev. B.*, 136:864, 1964.
- [34] W. Kohn and L. Sham. Self-consistent equations including exchange and correlation effects. *Phys. Rev. A.*, 140:1133, 1965.
- [35] R. Wiesendanger. Observation of vacuum tunneling of spin-polarized electrons with the scanning tunneling microscope. *Phys. Rev. Lett.*, 65(2):247, 1990.
- [36] J.K. Gimzewski, B. Reihl, J.H. Coombs, and R.R. Schlittler. Photon emission with the scanning tunneling microscope. *Zeitschrift fur Physik B*, 72:497, 1988.
- [37] M. Sakurai, C. Thirstrup, and M. Aono. New aspects of light emission from stm. *Applied Physics A*, 80:1153, 2005.
- [38] S. Ushioda. Probing individual nanostructures with stm-induced light emission. *Solid State Communications*, 117:159, 2001.

- [39] S.F. Alvarado, Ph. Renaud, D.L. Abraham, Ch. Schonenberger, D.J. Arent, and H.P. Meier. Luminescence in scanning tunneling microscopy on III-V nanostructures. *J. Vac. Sci. Technol. B*, 9(2):409, 1990.
- [40] R. Berndt, J. K. Gimzewski, and P. Johansson. Inelastic tunneling excitation of tip-induced plasmon modes on noble-metal surfaces. *Phys. Rev. Lett.*, 67:3796, 1991.
- [41] G. Hoffmann, T. Maroutian, and R. Berndt. Color view of atomic highs and lows in tunneling induced light emission. *Phys. Rev. Lett.*, 93:076102, 2004.
- [42] A. Downes and M. E. Welland. Photon emission from Si(111)-(77) induced by scanning tunneling microscopy: Atomic scale and material contrast. *Phys. Rev. Lett.*, 81:1857, 1998.
- [43] S. Ushioda. Scanning tunneling microscope (stm) light emission spectroscopy of surface nanostructures. *J. Electron Spectrosc. Relat. Phenom.*, 109:169, 2000.
- [44] C. Thirstrup, M. Sakurai, K. Stokbro, and M. Aono. Visible light emission from atomic scale patterns fabricated by the scanning tunneling microscope. *Phys. Rev. Lett.*, 82:1241, 1999.
- [45] G. Hoffman, L. Libioulle, and R. Berndt. Tunneling-induced luminescence from adsorbed organic molecules with submolecular lateral resolution. *Phys. Rev. B* 65, 65:212107, 2002.
- [46] X.H. Qiu, G.V. Nazin, and W. Ho. Vibrationally resolved fluorescence excited with submolecular precision. *Science*, 299:542, 2003.
- [47] S. F. Alvarado. *NATO Ser. E*, 242:361, 1993.
- [48] A.L. Vazquez de Parga and S.F. Alvarado. Magnetic circular dichroism in cobalt films observed with scanning-tunneling-microscope-excited fluorescence. *Phys. Rev. Lett.*, 72:3726, 1994.
- [49] A.L. Vazquez de Parga and S. F. Alvarado. Circular dichroism in stm-excited luminescence on metals. *Europhysics Letters*, 36(8):577, 1996.
- [50] Ph. Renaud and S.F. Alvarado. Observation of spin-polarized-electron tunneling from a ferromagnet into GaAs. *Phys. Rev. Lett.*, 68:1387, 1992.
- [51] J.L. Moran-Lopez and J.M. Sanchez. *New Trends in Magnetism Magnetic Material and Their Applications*. Plenum, New York, London, 1994.
- [52] H. Hoche H.J. Elmers, J. Hauschild, U. Gradmann, D. Heuer H. Bethge, and U. Kohler. Submonolayer magnetism of fe(110) on w(110): Finite

- width scaling of stripes and percolation between islands. *Phys. Rev. Lett.*, 73:898, 1990.
- [53] J. Hauschild H. J. Elmers and U. Gradmann. Critical behavior of the uniaxial ferromagnetic monolayer Fe(110) on W(110). *Phys. Rev. B*, 54:15224, 1996.
- [54] H.J. Elmers. Magnetization states in ultrathin films with laterally modulated anisotropies. *J. Magn. Magn. Mater.*, 185:274, 1998.
- [55] J. Hauschild and U. Gradmann and H.J. Elmers. Dipolar antiferromagnetism in double layer nanostripe arrays of Fe(110) on W(110). *Appl. Phys. Lett.*, 72:3688, 1998.
- [56] H.J. Elmers, J. Hauschild, and U. Gradmann. Onset of perpendicular magnetization in nanostripe arrays of Fe on stepped W(110) surfaces. *Phys. Rev. B*, 59:3688, 1999.
- [57] H. Bethge, D. Heuer, C. Jensen, K. Reshoft, and U. Kohler. Misfit-related effects in the epitaxial growth of iron on W(110). *Surf. Sci.*, 331:878, 1995.
- [58] J. Hauschild H. J. Elmers, H. Hoche, and U. Gradmann. Submonolayer magnetism of Fe(110) on W(110): Finite width scaling of stripes and percolation between islands. *Phys. Rev. Lett.*, 73:898, 1994.
- [59] *Instruction Manual UHV Evaporator EFM 3/3s/4*. Omicron NanoTechnology, 2005.
- [60] O. Pietzsch, A. Kubetzka, M. Bode, and R. Wiesendanger. Real-space observation of dipolar antiferromagnetism in magnetic nanowires by spin-polarized scanning tunneling spectroscopy. *Phys. Rev. Lett.*, 84(22):5212, 2000.
- [61] Tectra, Reuterweg 65, D-60323 Frankfurt/M, Germany, tel +49 (0)69-720040, fax +49 (0)69-720400, info@tectra.de.
- [62] PLM GmbH und Co.KG, Am Wasenbrunnen 12, 75242 Neuhausen, Germany, tel. +49-7234-980692, fax +49-7234-980693, www.pl-mechanik.de.
- [63] Emil C. Gerber und Soehne, Ginsterweg 1, D-55715 Idar-Oberstein.
- [64] R. Cortenraad, S.N. Ermolov, A.W. Denier van der Gon, V.G. Glebovskii, H.H. Brongersma, and A. Manenschijn. Cleaning procedure for single-crystal tungsten substrates. *Inorganic Materials*, 37(7):673, 2001.
- [65] R.G. Musket. Room-temperature adsorption of oxygen on tungsten surfaces – a review. *J. Less-common Metals*, 22:175, 1970.

- [66] L.W. Anders and R.S. Hansen. Mixed adsorption of carbon monoxide and oxygen on tungsten (100), (110), and (111) single crystal faces. *Journal of Chemical Physics*, 62(12):4652, 1974.
- [67] A. Elbe, G. Meister, and A. Goldmann. Vibrational modes of atomic oxygen on w(110). *Surf. Sci.*, 137:438, 1997.
- [68] K.E. Johnson, R.J. Wilson, and S. Chiang. Effects of adsorption site and surface stress on ordered structures of oxygen adsorbed on w(110). *Phys. Rev. Lett.*, 71:1055, 1993.
- [69] D.M. Bruls. *Direct profiling of III/V semiconductor nanostructures at the atomic level by cross-sectional Scanning Tunneling Microscopy*. PhD thesis, University of Technology Eindhoven, 2003.
- [70] P. Offermans. *Study of III-V semiconductor nanostructures by cross-sectional scanning tunneling microscopy*. PhD thesis, University of Technology Eindhoven, 2005.
- [71] A.M. Yakunin. *Mn in GaAs studied by X-STM: from a single impurity to ferromagnetic layers*. PhD thesis, University of Technology Eindhoven, 2005.
- [72] G.J. de Raad, P.M. Koenraad, and J.H. Wolter. Use of the schiller decapitation process for the manufacture of high quality tungsten scanning tunneling microscopy tips. *Journ. Vac. Sci. Tehc. B*, 17, 1999.
- [73] G.J. de Raad. *Voltage-dependent Scanning Tunneling Microscopy on the 110-surfaces of GaAs, AlGaAs and their heterostructures*. PhD thesis, University of Technology Eindhoven, 2001.
- [74] M. Bode, R. Pascal, and R. Wiesendanger. Scanning tunneling spectroscopy of Fe/W(110) using iron covered probe tips. *J. Vac. Sci. Technol. A*, 15(3):1285, 1997.
- [75] M. Bode. Spin-polarized scanning tunnelling microscopy. *Rep. Prog. Phys.*, 66:523, 2003.
- [76] A. Kubetzka. Spinpolarisierte rastertunnelmikroskopie an magnetischen nanostrukturen: Fe/w(110). *Dissertation zur Erlangung des Doktorgrades des Fachbereichs Physik der Universitt Hamburg*, 2002.
- [77] M. Kemerink, J.W. Gerritsen, J.G.H. Hermsen, P.M. Koenraad, H. van Kempen, and J. H. Wolter. Low-temperature scanning-tunneling microscope for luminescence measurements in high magnetic fields. *Rev. Sci. Instrum.*, 72:132, 2001.